BNL-108011-2015-JA

Cloud microphysical relationships and their implication on entrainment and mixing mechanism for the stratocumulus clouds measured during the VOCALS project

[1]Seong Soo Yum, [2]Jian Wang, [2]Yangang Liu, [2]Gunnar Senum, [2]Stephen Springston, [2]Robert McGraw and [1]Jae Min Yeom
[1]Department of Atmospheric Sciences, Yonsei University, Seoul 120-749, Korea
[2]Atmospheric Sciences Division, Brookhaven National Laboratory, Upton, New York 11973-5000, USA

Revised for publication in Journal of Geophysical Research
February 28, 2015

Corresponding author:
Dr. Seong Soo Yum
Department of Atmospheric Sciences
Yonsei University
Seoul 120-749, Korea

Fax: 82-2-365-5163
E-mail: ssyum@atmos.yonsei.ac.kr

Abstract
Cloud microphysical data obtained from G-1 aircraft flights over the southeastern pacific during the VOCALS-Rex field campaign were analyzed for evidence of entrainment mixing of dry air from above cloud top. Mixing diagram analysis was made for the horizontal flight data recorded at 1 Hz and 40 Hz. The dominant observed feature, a positive relationship between cloud droplet mean volume (V) and liquid water content (L), suggested occurrence of homogeneous mixing. On the other hand, estimation of the relevant scale parameters (i.e., transition length scale and transition scale number) consistently indicated inhomogeneous mixing. Importantly, the flight altitudes of the measurements were significantly below cloud top. We speculate that mixing of the entrained air near the cloud top may have indeed been inhomogeneous; but due to vertical circulation mixing the correlation between V and L became positive at the measurement altitudes in mid-level of clouds, because during their descent, cloud droplets evaporate, faster in more diluted cloud parcels, leading to a positive correlation between V and L regardless of the mixing mechanism near the cloud top.

1. Introduction

In warm clouds, after cloud droplets are formed, their growth to precipitation size occurs in two steps: first they grow by vapor diffusion, then some of the lucky ones grow large enough to initiate the collision and coalescence process, triggering further growth to precipitation drops. According to the adiabatic condensational droplet growth theory, however, it takes too long for the droplets to reach sizes (circa 50 μm) needed to initiate the collision – coalescence process, when compared to observed precipitation times that can be less than 30 min after cloud formation [*Rogers and Yau*, 1989]. Furthermore, observed cloud droplet spectra typically broaden with time as the droplets grow [e.g., *Hudson and Yum*, 1997], which is in dire contrast to the narrowing predicted by diffusion-controlled growth theory [*Rogers and Yau*, 1989]. These fundamental discrepancies between observation and theory have been a puzzle in cloud physics community for several decades, during which time there have been many explanations proposed to resolve them, as summarized by *Beard and Ochs* [1993] and more recently by *Devenish et al.* [2012] and *Grabowski and Wang* [2013].

These recent reviews emphasized the role of turbulence, especially at small-scales, in cloudy environments. Small scale turbulence fluctuations in cloud, the length scale of which may become close to the Kolmogorov microscale (η; ~ 1 mm), can cause the fluctuations in droplet distribution and therefore in the supersaturation field. Although still controversial, it was claimed that the influence of these fluctuations contributed little to the droplet spectral broadening during the condensational growth, due to rapid readjustment of the droplet distribution and the supersaturation field. That is, cloud droplets do not stay under the same supersaturation condition long enough to cause significant variation of their sizes [*Vaillancourt et al.*, 2002]. Effects from turbulence-induced fluctuations in water vapor saturation ratio on cloud droplet growth were also examined using a stochastic Brownian drift-diffusion model. Estimates of the correlation time, ranging from several seconds to tens of seconds, suggest that fluctuations in saturation ratio are strongly damped over the time scale, τ (on order of several minutes), required for significant change in the cloud droplet distribution. Nevertheless, both Monte-Carlo and analytic calculations support broadening under these conditions to a Weibull-shaped cloud droplet size distribution on time scales of several τ [*McGraw and Liu*, 2006]. Turbulence-induced fluctuations in in-cloud saturation ratio and the resulting fluctuations in cloud droplet growth rate were also shown to accelerate the formation of warm rain [*McGraw and Liu*, 2003; 2004].

Several numerical model studies demonstrated that warm rain initiation time could be shortened when the effect of small-scale turbulence on enhancement of the collision process was taken into account [*Xue et al.*, 2008; *Wang and Grabowski*, 2009; *Grabowski and Wang*, 2009; *Seifert et al.*, 2010]. However, the turbulent collision kernels used in these studies could be the lower bound of what might occur in real clouds as *Devenish et al.* [2012] pointed out, since they were estimated under much lower flow Reynolds number regime than could be found in real clouds and therefore could not account for all scales of turbulence affecting droplet-droplet interactions. This could imply that collisional droplet growth in these studies could have been shortened even more if more realistic collision kernels were used. Moreover, if the small scale turbulence allow a droplet to move from one larger scale eddy to another that has different growth history and supersaturation field, this could eventually lead to a significant spectral broadening [*Cooper et al.,* 1989; *Lasher-Trapp et al.,* 2005]. Still the question is whether or not this acceleration is fast enough to fully explain the gap between the observation and theoretical calculations based on the assumption of adiabatic condensational droplet growth.

Turbulence is also responsible for generating large eddies and entraining clear air into the cloud. Several ideas were proposed on how the entrained air is mixed with the cloudy air. When the mixing time scale (τ_m) is much shorter than the evaporation time scale (τ_e), mixing would occur first and evaporation of droplets in the mixed volume would follow. In the opposite case, complete evaporation of the droplets would occur first at the interfacial region between cloudy and entrained clear air, helping to achieve saturation, and mixing would follow without immediate change in the droplet size distribution. The former case is called homogeneous mixing [HM; *Warner,* 1973] and the latter inhomogeneous mixing [IM; *Baker et al.,* 1980]. Buoyancy difference of the mixed parcel from the surrounding cloudy air may also induce vertical circulation and the droplet spectrum may change subsequently [e.g., *Telford and Chai,* 1980; *Wang et al.,* 2009]. The immediate result of HM is the dilution of cloud water mixing ratio and droplet concentration, followed by decrease in droplet size through evaporation. Therefore HM could actually delay droplet growth instead of accelerating it. On the other hand IM could result in even greater reduction in droplet concentration, due to complete evaporation of some of the droplets, in addition to the dilution, but no immediate change in the droplet spectrum. With the reduced droplet concentration, further ascent of IM-affected cloud parcel may produce larger droplets than would be expected from an adiabatic cloud parcel.

Unlike small scale turbulence, the effects of which are difficult to be confirmed observationally, the effect of entrainment and mixing on the cloud droplet distribution can be inferred from aircraft observation of cloud microphysics. Significant variations of droplet concentration without change in droplet spectral shape were suggested as evidence for IM [e.g., *Paluch and Knight,* 1984; *Paluch,* 1986] and this was usually the case for stratocumulus clouds [e.g., *Burnet and Brenguier*, 2007; *Haman et al*., 2007; *Lu et al*., 2011]. Similar behavior has been found in some cumulus clouds [e.g., *Gerber et al*., 2008; *Lehmann et al*., 2009] but cumulus clouds seemed more prone to HM. *Yum and Hudson* [2001] found a predominantly positive correlation between droplet concentration and mean diameter for the cumulus clouds observed during the Small Cumulus Microphysics Study (SCMS) project [*Knight and Miller*, 1998], which could be interpreted as evidence for HM. Using a mixing diagram, *Burnet and Brenguier* [2007] also showed that the SCMS clouds were more likely to be affected by HM and indeed the ratio of the two time scales, τ_m/τ_e, known as the Damkohler number (Da), could be an important parameter to check to see if mixing was homogenous or inhomogeneous as originally proposed by *Baker et al*. [1980]: Da << 1 for the SCMS cumulus clouds, and Da >> 1 for the examined stratocumulus clouds suggestive of IM. *Lehmann et al*. [2009] went further to demonstrate that a single Da was not sufficient and a transition length scale (J^*) should be introduced to properly set a criterion for HM and IM. *Lu et al*. [2011] advanced this idea and proposed the transition scale number (J_L), which is the ratio of J^* to η, as a dynamical measure of homogeneous mixing degree.

The important point, however, is that evidence for enhanced droplet growth after IM (i.e., larger droplets in more diluted cloud region) is not easily found. *Lehman et al*. [2009] and *Lu et al*. [2011] did find such trend in some cloud penetrations, but more prevalently it was the near adiabatic cloud parcels with high droplet concentration that had the largest droplets [e.g., *Paluch and Knight*, 1984; *Paluch and Baumgardner*, 1989]. *Yum and Hudson* [2001] also convincingly showed that not only in the SCMS cumulus clouds, but also in the stratocumulus clouds measured during several other aircraft campaigns, the correlation between droplet concentration and mean diameter was positive in a large portions of the datasets. This apparent lack of evidence for so called super-adiabatic droplets [*Blyth and Latham*, 1985] in diluted cloud parcels seems to suggest that mixing of entrained air may not generally promote droplet growth.

In this study we examine this problem for the stratocumulus clouds observed over the Southeastern Pacific. The mixing diagram of *Pawlowska et al*. [2000], which was later advanced by *Burnet and Brenguier* [2007], is used to illustrate the cloud microphysical relationships, although inferences from this diagram depends on the amount and thermodynamic properties of entrained air, which cannot be accurately known. The estimated values of Da, J^* and J_L for these clouds consistently indicate that IM should be dominant as the environmental conditions for stratocumulus clouds usually do [e.g., *Burnet and Brenguier*, 2007]. However, the mixing diagram plots do not generally support these indications and in fact suggest HM dominance. We speculate that the mixing of entrained air near the cloud top was inhomogeneous but vertical circulation mixing in clouds [*Wang et al*., 2009] modulated the cloud microphysical relationships to suggest HM dominance.

2. Data

The data used in the present study were obtained during G-1 aircraft measurements of marine boundary layer stratocumulus clouds taken over the southeastern Pacific off the coast of Chile during the VAMOS Ocean-Cloud-Atmosphere-Land Study Regional Experiment (VOCALS-REx) field campaign [*Wood et al*., 2011]. There were 17 G-1 flights during VOCALS-Rex and the data from three flights on Oct. 17, 26 and 28, 2008 (O17, O26 and O28) are analyzed in this study.

Cloud droplet (2 μm < D < 50 μm) size distributions were measured by a Cloud and Aerosol Spectrometer (CAS) probe manufactured by Droplet Measurement Technologies (DMT). The data were archived at various sampling rates. This study makes use of the 1 Hz and 40 Hz data. For the 1 Hz data the CAS probe has 20 bins covering 0.6 to 56.3 μm D range, but only the larger 11 bins that cover 1.66 to 56.3 μm D range are counted to consider only the activated cloud droplets. The 40 Hz data were derived from 200 Hz Particle by Particle data stream and were classified into 100 bins between 2- 50 μm. Drizzle drops (D > 50 μm) were measured by a Cloud Imaging Probe (CIP) by DMT that covers the D range of 7.5 to 937.5 μm but the first three bins that overlap with the CAS probe are discarded to confine the range 52.5 to 937.5 μm D. Integration of the CAS size distribution produces the liquid water content (LWC) of cloud droplets (L). The LWC of drizzle drops (L_d) are similarly obtained by integrating the CIP size distributions. In addition, cloud liquid water content was separately measured by a Particle Volume Monitor (PVM) and by a hot wire LWC sensor, but for consistency here only the CAS probe data are used.

Assuming an aircraft speed of 100 m s^{-1}, the 1 Hz and 40 Hz sampling rates correspond to 100 m and 2.5 m resolution, respectively. For the same aircraft speed, the volumetric sampling rate of the CAS probe is 14 cm^3 s^{-1}. We used LWC = 0.001 g m^{-3} as the threshold value for deciding cloud samples, meaning that all samples with LWC < 0.001 g m^{-3} were neglected as non-cloud samples. This is equivalent to N = 2 cm^{-3} when droplet diameter is assumed to be 10 μm. This would not pose any problem for 1 Hz data but applying the same threshold for 40 Hz data could cause problem. The sample volume is 14/40 = 0.35 cm^3 for each 40 Hz sample. To make sure at least one droplet present in cloud samples, we applied N = 3 cm^{-3} threshold when we processed the 40 Hz dataset. Then LWC = 0.001 g m^{-3} threshold was applied to these 40 Hz dataset for consistency with the 1 Hz dataset.

3. Mixing diagram

Pawloska et al. [2000] used a mixing diagram to show cloud microphysical relationships during horizontal penetrations of stratocumulus clouds. The mixing diagram is comprised of the two axes, N/N_a and D_v^3/D_{va}^3, where N and D_v are cloud droplet number concentration and mean volume diameter, respectively, and the subscript 'a' indicates the adiabatic value. Therefore N/N_a and D_v^3/D_{va}^3 represent relative deviations from the adiabatic values. The mean volume of cloud droplets can be expressed as V (= $\pi D_v^3/6$) and its adiabatic value as V_a (= $\pi D_{va}^3/6$). Then V/V_a can replace D_v^3/D_{va}^3 in the mixing diagram. Since

$$L = NV \tag{1}$$

and

$$La = NaVa \tag{2}$$

are defined, the cloud droplet LWC dilution ratio (α) can be calculated as

$$\alpha = \frac{L}{La} = \frac{N}{Na}\frac{V}{Va} \tag{3}$$

and therefore α = const (iso-α) lines can be drawn in the diagram as rectangular hyperbolas. Then the data plotted in the diagram can also indicate the relative deviation from L_a. *Burnet and Brenguier* [2007] advanced this diagram by putting the lines that represent the variation of N/N_a and V/V_a when environmental dry air is mixed homogeneously with the adiabatic cloudy air. These lines are determined by the heat and moisture balance equations for the mixture. Let T_a, $q_{vs}(T_a)$ and q_{la} be the temperature, saturation vapor mixing ratio and liquid water mixing ratio of the adiabatic cloudy air, respectively, and T_e and RH be the temperature and relative humidity of the entraining environmental dry air, respectively. If the volume fraction of the cloudy air is χ, then the temperature and liquid water mixing ratio of the homogeneously mixed air, T and q_l, can be expressed as

$$\mathrm{T} = \left(Ta\text{-}\mathrm{T}e\text{-}\mathrm{qla}\frac{Lv}{Cp} \right)\chi + \mathrm{T}e + \mathrm{q}l\frac{Lv}{Cp} \tag{4}$$

and

$$ql = \chi\left[q\mathrm{la}\text{-}\mathrm{qvs}\left(Te\right)\mathrm{RH} + \mathrm{qvs}\left(Ta\right) \right] + \mathrm{qvs}\left(Te\right)\mathrm{RH}\text{-}\mathrm{qvs(T)}\ , \tag{5}$$

where L_v and C_p are the latent heat of vaporization and the specific heat at constant pressure, respectively. The underlying assumptions for Eqs. (4) and (5) are that the adiabatic cloudy air is just saturated and the mixing is isobaric (i.e., the pressures (p) of the cloudy air and environmental dry air are the same). It is obvious that Eqs. (4) and (5) can only be solved by iteration. For HM, $\chi = N/N_a$ is understood. Once q_l is known, then V/V_a can be obtained from Eq. (3) since $q_l/q_{la} = L/L_a$.

Figure 1 is an example of the mixing diagram setting. If IM occurs, N would reduce from N_a by the proportion of χ but V would maintain the adiabatic value of V_a. Therefore the mixed parcels that are subject to IM would produce the data points that will line up on the V/V_a =1 line. If the IM affected cloud parcels experience further growth as was postulated by *Baker et al*. [1980], cloud droplets may grow larger than the sizes expected from the adiabatic condensational growth, which is the key argument for IM being an accelerating droplet growth mechanism. It could be claimed as evidence for that if observed V/V_a is becoming larger than one as N/N_a decreases, an example of which is shown in Fig. 1. On the other hand, if HM occurs, where the data points line up will be dependent on RH as well as on the other thermodynamic variables that appear in Eqs. (4) and (5). The RH=const (iso-RH) lines shown in Fig. 1 are the examples for a particular set of thermodynamic variables: T_a = 285.3 K, T_e = 292.9 K and p = 942 hPa. The large difference between T_a and T_e is typical of the subtropical stratocumulus topped marine boundary layer, above which the air is much warmer and drier, as is also the case for the VOCALS clouds (shown later). If RH is lower for the entraining environmental air, evaporation of the droplets would be more efficient and thus the size of the droplets would decrease faster as HM occurs: the lower the RH the steeper the slope of the iso-RH line. For the extreme cases of very high RH (i.e., close to 100%), HM could actually result in supersaturation and therefore droplet growth (see RH=99% line in Fig. 1). However, in reality this would rarely occur in the subtropical stratocumulus topped marine boundary layer where the air is usually very dry above the boundary layer.

Despite the fact that the mixing diagram can illustrate a number of microphysical relationships and provide insight on how the mixing of entrained air proceeds, it has limitations. Having a proper estimate of N_a and V_a is critical for the mixing diagram analysis. In real clouds, however, the updraft speed near cloud base, which determines the activated cloud droplet concentration, could vary and therefore N_a may not have a single value throughout the cloud as recognized by *Jensen et al*. [1985]. If so, V_a at a constant height from cloud base cannot be maintained as a single value for the cloud. Cloud base altitude could also vary for a cloud of large horizontal dimension such as marine stratocumuli [e.g., *Wang et al.*, 2009]. This means that even if the cloud is strictly adiabatic and the updraft speed is uniform, V_a at a constant altitude may not be a single value for this cloud. For a cloud penetration at a constant altitude, the adiabatic cloud parcels are supposed to reside at the point (N/N_a=1, V/V_a =1) in Fig. 1, but if there are variations in N_a, and thus V_a, this is not possible and great care needs to be taken when analyzing the data.

4. Results

4.1 1 Hz data

Figure 2 shows the time variation of the important cloud microphysical parameters during the flight on October 28 (O28). All data are 1 s averages (1 Hz). The flight pattern shows that the aircraft is making long horizontal penetrations (marked as P1, P2…) and vertical soundings through the cloud layer (Fig. 2a) as it flies out westward off the Chilean coast (Fig. 2b). The CN and CCN concentrations (N_{CN} and N_{CCN}) gradually decrease with distance from the coast, where pollution sources are present [*Kleinman et al.*, 2012]. N shows the same trend (Fig. 2b). V, on the other hand, becomes larger with the distance from the coast as does drizzle liquid water content (L_d) (Fig. 2a). The aerosol-induced modulation of cloud microphysics is clearly demonstrated during this flight but will not be discussed further here because the focus of the present study is on the cloud microphysical relationships.

Visible satellite image on this day was shown in *Wood et al*. [2001], which demonstrated that on this day the marine stratocumulus clouds over the southeastern Pacific Ocean were multi-structured with open cells far off the coast and closed cells closer to the coast. The G-1 aircraft flight track was confined within the closed cell region on this day but even within the closed cell region mesoscale structure was obvious in the satellite image, which is consistent with the significant variation of L within a horizontal penetration (Fig. 2). In this case, putting all data in an entire horizontal penetration in one mixing diagram can be problematic as shown later since there could be multiple numbers of N_a and V_a.

The vertical distribution of L measured during O28 is shown in Fig. 3a along with the vertical variation of T, dew point temperature (T_d) and liquid water potential temperature (θ_l.), which can be obtained following *Deardorff* [1980]

$$\theta_l = \theta - (\frac{\theta}{T}\frac{L_v}{C_p})q_l, \quad (6)$$

where θ is the potential temperature. It is clear that the air above the cloud top is very dry and much warmer than the inside of the cloud layer where L generally increases with altitude. The near uniform θ_l profiles below the inversions suggests that the air is well mixed below the cloud top but the various inversion altitudes of T and also of θ_l indicate that the cloud top altitudes vary significantly for these extensive stratocumulus clouds. We can also see that the cloud base altitude and thus L vary significantly and L varies too during horizontal penetrations at a constant altitude. Hypothetical L_a soundings that start from three different cloud base altitudes are drawn in Fig. 3a to illustrate the error in estimating V_a [from Eq. (2)] when the cloud base altitude is not correctly known. Moreover, unlike T and θ_l, which vary significantly and instantaneously as the aircraft moves in or out of the cloud layer, the variation in T_d is much more gradual due to the slow response time of the chilled mirror hygrometer to detect any abrupt change of moisture content. This makes the RH values derived from T_d somewhat uncertain at the altitudes near the cloud top. T_d measurement does become stabilized after this transitional time is passed but another problem noticeable in Fig. 3 is that T tends to be a few Kelvin lower than T_d during the horizontal penetrations, which is unexpectedly large because in stratocumulus clouds supersaturation is expected to be close to zero (i.e., T ~ T_d). The measured T appears to be biased low inside the cloud conceivably because of cooling by evaporation of cloud droplets upon their impact on sensor element.

Moreover, in most of the soundings, the existence of an entrainment interface layer (EIL) was evidenced by a jump in T above the cloud top that was not abrupt but had a finite transition depth. Then it is possible that the cloudy air is actually mixed with the air in the EIL zone [*Gerber et al*., 2005], where RH could be much higher than that above it. This makes it very difficult to identify the source altitude of the entrained air. A thermodynamic diagram (e.g., *Paluch* [1979]) can be used for this purpose but it is difficult because of the uncertainty in T and T_d measurements. So in this study we assume B as the source altitude of the entrained air, which is the mid-point of EIL in Fig. 3b that shows typical vertical structures of θ_l and q_T (= $q_{vs}(T_d)$ + q_l; total water mixing ratio). It is noteworthy that interpretation of the mixing diagram can be varied depending on where the entrained air comes from. If A in Fig. 3b is the case, RH of the entrained air can be very close to saturation and therefore identifying HM or IM would be difficult and meaningless. On the other hand, if C in Fig. 3b is the case, the entrained air would be very dry and therefore HM or IM would be distinctively identified in the mixing diagram. Lastly, the two most important parameters needed for estimating N_a are the CCN spectra and the updraft speed below the cloud base altitude, but these are not directly measured, and the estimation of them is difficult especially for the extensive clouds shown in Fig. 2.

Table 1 shows the averages of the important cloud parameters for each horizontal penetration. The average T and p at the penetration altitudes do not vary much during O17, O26 and O28. During the two horizontal penetrations (P2 and P4) in O28, the flight altitude changed somewhat or the data characteristics changed significantly in the middle of the penetration and therefore they were subdivided into two parts. The height of the penetration in cloud is estimated based on the vertical soundings of L taken just before or after the penetration and as shown in Table 1 the penetration heights are generally in the mid-level of the cloud but somewhat closer to cloud top than cloud base. As expected from Fig. 2, the average N decreases and the average V increases with the distance from the coast during O28 in Table 1. The average L_d is generally small for most penetrations except P5 and P6 of O28, where L_d is almost comparable to L. The loss of cloud liquid water due to drizzle precipitation makes it difficult to find N_a and V_a, which are important when constructing the mixing diagram. Therefore care must be given when interpreting the mixing diagrams for the penetrations with non-negligible drizzle amount.

Since θ_l is a conservative variable and there is a sudden increase of θ_l above cloud top (Fig. 2), entrainment and mixing of the air from above cloud top would leave its trace. That is, it is expected to see higher θ_l for more entrainment affected (i.e., more L diluted) cloud parcels. Figure 4 shows that this is indeed the case for all horizontal penetrations (only one subdivided part from P2 and P4 for brevity) perhaps except P3 of O28 (Fig. 4c): θ_l is higher for smaller L. The heights of these horizontal penetrations are not very close to cloud top (Table 1) but the evidence of cloud top entrainment seems to be retained clearly here. Shown together in Fig. 4 is the virtual potential temperature, θ_v, defined as [*Deardorff*, 1980],

$$\theta_v = \theta\left(1 + 0.61 q_v - q_l\right), \tag{7}$$

where q_v is the vapor mixing ratio. More diluted parcels tend to have lower θ_v in most penetrations in Fig. 4, indicating relatively more negative buoyancy for more diluted parcels. In conjunction with this, cloud top entrainment instability (CTEI) can be checked for these clouds. Several CTEI criteria have been proposed [*Yamaguchi and Randall*, 2007] but the one proposed by *Randall* [1980] and *Deardorff* [1980] is used most frequently, which states:

$$\Delta\theta_e - \kappa\left(\frac{L_v}{C_p}\right)\Delta q_T < 0 \tag{8}$$

as the CTEI criterion, where $\Delta\theta_e$ and Δq_T are the equivalent potential temperature [$\theta_e = \theta + (L_v/C_p)q_v$] and the q_T jump at the cloud top, respectively, and κ is the stability parameter, a proper value of which would be 0.23 for the T and P ranges observed during O17, O26 and O28 [*Yamaguchi and Randall*, 2007]. When $\Delta\theta_e$ and Δq_T were estimated with the θ_e and q_T at the middle of EIL (B in Fig. 3b) and the average θ_e and q_T for each horizontal penetration, the CTEI criterion were satisfied for all cases analyzed in this study (not shown). This does not necessarily imply the breakup of the cloud layer [*Gerber et al*., 2005] but it can be expected that the descent of the evaporatively cooled mixed parcels would not have been confined to the cloud top region. This is also consistent with the fact that more diluted parcels tend to have lower θ_v in most penetrations in Fig. 4. When C in Fig. 3b was used as the altitude of entrained air for all 8 cases in O28, the CTEI criterion was still satisfied in 5 cases but not in the remaining 3 cases..

Figure 5 shows the mixing diagrams for each of the corresponding six horizontal penetrations shown in Fig. 4. Some assumptions are necessary because of the difficulties and uncertainties mentioned above in estimating parameter values for the diagram. The maximum N and V (i.e., N_m and V_m) for each penetration are used as proxy values for N_a and V_a of the penetration, respectively.

For the calculation of iso-RH lines for HM, the average T for a horizontal penetration (Table 1) and the T at the mid-point of EIL (B in Fig. 3b) are assumed to be T_a and T_e, respectively. The average p for a horizontal penetration (Table 1) is assumed to be the pressure where mixing occurs. These assumptions may not be realistic, but they cause no problem when interpreting the mixing diagram. N_m and V_m are used only as scaling parameters. The iso-RH lines in Fig. 5 can be constructed by assuming C or A (Fig. 3b) as the source altitude of the entrained air. This would produce conspicuously different iso-RH lines for high RH values but not much so for low RH values. Moreover, finding the right source altitude and RH of the entrained air seems not to be critical because none of the six penetration cases in Fig. 5 shows an HM-like feature. Also displayed in Fig. 5, as color scale, is the information on the relative dispersion (ξ = standard deviation of diameter / mean diameter).

In all cases shown in Fig. 5, no data points exist where adiabatic parcels should reside, at the upper right corner ($N/N_m=1$, $V/V_m=1$). Moreover, the parcel with the highest N does not have the largest V. This might be explained by having multiple mixing regimes in most cases in Fig. 5, which are certainly related to a number of mesoscale structures shown in Fig. 2. For example, the data scatter for P1 (Fig. 5a) does not seem to lie within any of the mixing scenarios (see Fig. 1) and some section of the data are lined up almost parallel to iso-α lines (see especially Fig. 5f). Two possible scenarios for this latter behavior are either (1) that all the cloud parcels are close to adiabatic, and therefore maintain similar L values, while N and V vary roughly to satisfy the constraint of Eq. (1), because the updraft speeds are not the same for the different cloud parcels, or (2) that all the cloud parcels are subject to a similar degree of liquid water dilution but without noticeably disrupting the adiabatic N-V relationship. The former scenario should be much more likely than the latter one. However, the L values in the region where this behavior is seen are relatively small (Figs. 5a and 5f). The α values here are also comparatively small. The small L values may be due to a shorter height from cloud base for this section than for the rest of the penetration. Since the horizontal penetrations were made at a constant altitude, this could also mean that cloud base altitudes were higher for this section than for the rest of the penetration. P5 is a case that seems to indicate IM and further growth after IM (Fig. 5e). Worth mentioning here is that a similar data scatter can also be caused by entrainment and mixing of almost saturated air just above the cloud top (A in Fig. 3b), which *Gerber et al*. [2005] suggested as a possible explanation for such behavior. Lastly, it is clear that relative dispersion (ξ) generally becomes larger as α decreases, i.e., droplet spectra become broader for more diluted parcels [e.g., *Hudson and Yum*, 1997]. With the larger ξ for the diluted parcels in P5, some of the droplets in these parcels may indeed have attained super-adiabatic sizes.

Figure 6 shows the mixing diagrams for the two penetrations during O17, which were made over a very close geographical area but at two different cloud altitudes: close to cloud top and mid-level of cloud (Table 1). The times of the penetrations were not consecutive but seemed to be close enough to sample the same persistent stratocumulus deck. Interestingly, the data scatter for P1 (close to cloud top, Fig. 6a) clearly indicates IM and/or further growth after IM. Meanwhile, the data scatter for P2 (mid-level, Fig. 6b) seems to be of a pattern similar to those of Fig. 5b, 5c, and 5d. These contrasting results will be further discussed in the next section. Clearly demonstrated again in Fig. 6b is that ξ generally becomes larger as α decreases.

4.2 40 Hz data

It is clearly not appropriate to put all the data in a long horizontal penetration into one mixing diagram: Assuming the aircraft speed of 100 m s^{-1}, a 5 min horizontal penetration would cover a 30 km cloud path and the assumption of constant values for N_a and V_a would be inappropriate. Because the data shown in Figs. 5 and 6 are at 1 Hz, which are averages over 100 m cloud paths at this airspeed, and the scale of energy containing turbulent eddies are only up to about 100 m [*Grabowski and Wang*, 2013], important detail could be lost. One way to avoid these problems is to use a higher frequency in order to make the assumption of constant N_a and V_a more plausible, and construct the mixing diagram for each segment separately. Figure 7 shows the mixing diagrams for six consecutive 20 s segments taken from P1 of O28 with the 40 Hz data. Each 20 s segment represents 2 km long cloud path and each data point is an average over 2.5 m. As putting HM (iso-RH) lines in the diagrams does not add significant information, they are not drawn. Again N_m and V_m for each segment are used as proxies for N_a and V_a, respectively. Still there are no data points in the right upper corners of all six diagrams in Fig. 7, and the cloud parcels having highest values for N and V are not the same. As expected, however, the data scatter is much smaller than for the 1Hz P1 data shown in Fig. 5a. A few data points in the lower left portion of Fig. 7a suggest severe dilution and HM for these parcels. Otherwise no significant dilution is observed and the dispersion (ξ) is generally small for this 120 s (12 km) long cloud path (from Fig. 7a to Fig. 7f), and the N_m and V_m of the six segments (see the numbers in parentheses in x and y axis labels) are comparable to each other. Therefore it seems difficult to estimate how entrainment and mixing affected this cloud volume.

To examine more clearly how N/N_m and V/V_m vary with the liquid water dilution, Fig. 8 bins the α values into 0.05 intervals and the N/N_m and V/V_m values within each bin are averaged for the data shown in Fig. 7. Expected for an IM dominant case would be a decrease in N/N_m but no change in V/V_m with decrease in α. None of the six segments in Fig. 8 shows this trend; instead they show both N/N_m and V/V_m decreasing, indicative of HM. On the other hand, the very steep decrease of V/V_m compared to that of N/N_m, which is expected from HM of very dry environmental air (c.f. Fig. 1), is not found in any of the cases shown in Fig. 8.

Figure 7 is typical of the data scatter patterns found in the 20s-segment mixing diagrams analyzed in this study. Examples from some other frequently observed patterns are presented in Fig. 9 with the corresponding bin plots shown in Fig. 10. Fig. 9a shows limitedly scattered data within the range of α=0.1 to α=0.4 although the actual range of L is large for this segment: the largest L (α=0.4) is a factor of four larger than the smallest L (α=0.1). However, most of the data are concentrated around the α=0.2 iso-line and a negative correlation between N/N_m and V/V_m is obvious and results from the general inverse relationship between N and V within a limited range of L (Eq. (1)). If the inverse N-V relationship is due to further growth after IM, the data would scatter across the iso-α lines with the trend toward increasing V/V_m decreasing N/N_m (see Fig. 1). Notable is the wide variation of both N/N_m and V/V_m on an iso-α line, indicating considerable variation of N and V at constant L. The corresponding bin plot for this segment (Fig. 10a) shows a steep decrease in V/V_m with decrease of α, but no consistent variation of N/N_m. Fig. 9b looks similar to Fig. 9a but the α range is much larger and many data points are concentrated at the lower right corner of the plot, indicating that there are many cloud parcels of relatively very small L in this segment that have high concentration of very small cloud droplets. Speculatively this may be due to a high number of recently activated small cloud droplets in the cloud parcels that have small L. It is hard to tell what kind of mixing mechanism is dominant for this segment but the corresponding bin plot (Fig. 10b) shows a steep decrease of V/V_m and a slow decrease of N/N_m with decrease of α (except for the smallest two α bins), which resembles the data scatter expected for HM of very dry environmental air (see Fig. 1). There are relatively more diluted cloud parcels in Fig. 9c and the data scatter obviously suggest HM as confirmed by the corresponding bin plot in Fig. 10c. Meanwhile, Fig. 9d seems to indicate IM but its bin plot (Fig. 10d) still shows the decreasing trend of V/V_m with the decrease of α, suggesting that the mixing is not strictly inhomogeneous but remains homogeneously affected.

Figures 7 and 9 demonstrate that the data scatter patterns in the mixing diagrams can differ greatly across these 20 s (~ 2 km) segments of the VOCALS stratocumulus clouds. Cloud microphysical relationships from O17, O26 and O28 are summarized in Table 2. Here the correlation coefficients (Γ) for linear regressions between N and V, N and L, and V and L are calculated for each 20 s segment and averaged for each horizontal penetration. The numbers in parentheses are the averages of the Γ values for each 1 s segment (i.e., 40 data points for each segment) and will be discussed later. Shown together in Table 2 are the Γ values calculated for all 1 Hz data from each penetration. Additionally Fig. 11 shows how the $\Gamma_{N\text{-}V}$, $\Gamma_{N\text{-}L}$ and $\Gamma_{V\text{-}L}$ values for each segment paired with each other. Unfortunately, 40 Hz data were not available for O17. So the values in 40 Hz columns for O17 in Table 2 and the panels for O17 in Fig. 11 were calculated from the 20 s segments of 1 Hz data (i.e., only 20 data points for each segment). The average $\Gamma_{N\text{-}V}$ at 40 Hz for each penetration is mostly negative while the average $\Gamma_{N\text{-}L}$ and $\Gamma_{V\text{-}L}$ are dominantly positive in Table 2. A notable feature is the banded distribution of $\Gamma_{V\text{-}L}$ values in Figs. 11a, 11b and 11c: $\Gamma_{V\text{-}L}$ increases from the upper left to the lower right direction. This may be expected: if N and V are more negatively correlated, a larger $\Gamma_{N\text{-}L}$ would necessarily indicate lower $\Gamma_{V\text{-}L}$, and vice versa. Similar banded distributions are shown in Figs. 11d-11f and Figs. 11g-11i, reflective of the relationship L = NV.

The interrelationships shown in Fig. 11 have deep implications for the mixing mechanisms. Table 3 summarizes the expected correlation coefficient criteria for the different mixing mechanisms. If HM is dominant, all three Γ values are expected to be positive (see Fig. 1) and there are 47 such segments out of 303 from O17, O26 and O28 combined. Similarly no correlations between N and V and between L and V are expected if IM is dominant, and if further growth of the droplets in IM-dominated diluted cloud parcels does occur, negative $\Gamma_{N\text{-}V}$ and $\Gamma_{L\text{-}V}$ would be expected. No segment satisfies the criteria for IM but there are 10 segments that support further growth after IM in Table 3. If new droplet activation occurs frequently in the small L parcels, as suggested in Fig. 9b, negative $\Gamma_{N\text{-}V}$ and $\Gamma_{N\text{-}L}$ but a positive $\Gamma_{V\text{-}L}$ would be expected and there are 43 such segments (Table 3). Lastly, when there is relatively small variation of L for a majority of the data in a 20 s segment, a strongly negative $\Gamma_{N\text{-}V}$ is expected as in Fig. 8a. These are the most frequently found cases in this study. The important point is that most of these segments show strong positive $\Gamma_{V\text{-}L}$ and $\Gamma_{N\text{-}L}$. The number of segments that meet these criteria is 169 in Table 3, which is 56% of all segments! Clearly the droplets are smaller and their concentration is generally lower in more diluted parcels although the L variation is small enough to produce a strongly negative $\Gamma_{N\text{-}V}$ in these cloud segments. Even in the cloud segments that seem to suggest IM (Fig. 9d), both $\Gamma_{N\text{-}L}$ and $\Gamma_{V\text{-}L}$ are positive as the corresponding bin plot indicates (Fig. 10d). Ultimately $\Gamma_{V\text{-}L}$ is positive in all segments with the exception of some segments in O17 (Fig. 11). That is, droplets are smaller in more diluted parcels for the majority of all of the cloud segments analyzed in this study. The question is whether these findings indeed suggest the prevalence of HM.

5. Discussion

The results shown above consistently suggest that the mixing of the entrained air follows HM, which is not a trait that promotes accelerated growth of cloud droplets. HM is also not consistent with the mixing mechanism expected from the analysis of relevant scale parameters as next discussed. Instead of using the evaporation time scale τ_e in defining the Damkohler number, *Lehmann et al*. [2009] proposed that using the reaction time scale (τ_r) is more appropriate in calculation of Da:

$$\mathrm{Da} = \frac{\tau_m}{\tau_r} = \frac{(L_E^2 / \epsilon)}{\tau_r} \ , \tag{9}$$

where L_E is the length scale of entraining eddy and ε is the turbulent dissipation rate. *Lehmann et al*. [2009] defined τ_r as either the time required for complete evaporation of the droplets or the time at which the saturation ratio is restored to 0.995. Since the droplet sizes and the saturation ratio change interactively during the evaporation of the droplets in the mixed volume, τ_r can only be calculated numerically. The difficulty lies in the calculation of τ_m because L_E can differ greatly for different clouds. Instead of calculating Da based on a rough guess of L_E, *Lehmann et al*. [2009] proposed using the length scale that sets Da to unity and named it the transition length scale, J^*. For entraining eddy length scales larger than J^*, Da will exceed unity and IM would be dominant, otherwise HM would be expected. Larger values of J^* indicates a greater chance for HM and vice versa. A dimensionless number, J_L, that includes both J^* and η [*Lu et al*., 2011] is defined as

$$J_L = \frac{L^*}{\eta} = \frac{L^*}{(\nu^3 / \epsilon)^{1/4}} \ , . \tag{10}$$

where ν is the kinematic viscosity. Larger J_L corresponds to a higher degree of HM and *Lu et al*. [2011] suggested 50 as the threshold value of J_L for homogeneous mixing.

Figure 12 shows the distributions of J^* and J_L for all 40 Hz data from P1 of O28. Table 4 shows the average, 5% percentile, median and 95% percentile values of these quantities for the penetrations during O26 and O28. Due to unavailability of 40 Hz data, these values were not calculated for O17. For these calculations, the average T and for each penetration are used and the saturation ratio is calculated based on the T, T_d and p values at the middle of the EIL (B in Fig. 3b). Together with these values, the number concentration and mean diameter of the droplets, and the ε for each 40 Hz datum (~2.5 m path) are used to calculate τ_m and τ_r, to give the J^* and J_L distributions shown in Fig. 12 and Table 4. The ε is calculated from the aircraft's true airspeed measured during the flight [*Poellot and*

Grainger, 1991] as explained in *Lu et al*. [2011], and ranged 10-100 $cm^2\ s^{-3}$ for the clouds analyzed in this study. Over 95% of the J^* values are less than 1 cm (Fig. 12a) suggesting that IM should be dominant in these clouds as the scale of entraining eddies are highly likely to be larger than 1 cm. Table 4 indicates similar results for all penetrations in O26 and O28. This behavior is in fact expected because it is very dry above the cloud top for all penetrations, and therefore τ_r is determined by the droplet evaporation time, which is very short. It would have been even shorter were the saturation ratio above EIL used instead of a value in the middle of the EIL. The J_L distribution for P1 of O28 in Fig. 12b shows a similar trend: more than 50% of the J_L values are smaller than unity and all values are less than 10, except a few outliers, which are still much smaller than the HM threshold of 50 suggested by *Lu et al*. [2011]. The trend is similar for all other penetrations shown in Table 4 and it is likely that O17 would have shown similar results had the 40Hz data been available to calculate J^* and J_L properly. These scale parameter analysis results are inconsistent with the results of the mixing diagram analysis that dominantly suggests a trait of HM.

Another important factor that affects cloud microphysical relationships is drizzle. The reasoning behind the mixing diagram is based on the assumption that the drizzle amount is negligible, meaning that the collision process is not so active as to distort the cloud microphysical relationships. The immediate effect of the collision process would be the preferential collection of larger cloud droplets due to their higher efficiency for collision with drizzle drops [*Yum*, 1998]. That is, larger droplets would be preferentially removed from the droplet population and transferred to the drizzle population. For the three flights analyzed here, only in P5 and P6 of O28 a significant amount of drizzle is observed (Fig. 1). The cloud microphysical relationships in these two penetrations (Table 2), however, do not seem to differ significantly from those in the other penetrations. The scale parameters, J^* and J_L, are noticeably larger for these two penetrations (Table 4) but that was because cloud droplets are larger (Table 1) and therefore τ_r are larger for these two penetrations. There are other aspects to be considered but these will not be discussed further in this study. In any case, it seems difficult to estimate the effects of drizzle on the microphysical relationships of cloud droplets.

The crucial assumption behind the mixing diagram is a uniform cloud base altitude for the data presented in the diagram. Basically L and V increase with height from cloud base in adiabatic clouds. If cloud base altitude varies, L and V would not be uniform even for a horizontal penetration through an adiabatic cloud that develops under a uniform updraft speed and this would pose an intrinsic problem in the mixing diagram analysis. One of the reasons for dividing up the data into 20 s (~2 km cloud path) segments in this study is to minimize this problem. Nevertheless, cloud base altitudes could still vary within a 20 s segment and the observed cloud microphysical relationships might include the influence of this variation. For the stratocumulus clouds analyzed in this study, more diluted parcels tend to have higher θ_l and lower θ_v (Fig. 4), suggesting that the dilution is caused by the entrainment of much drier and warmer air (i.e., high θ_l air) from above cloud top and the more diluted parcels become relatively less buoyant due to more evaporative cooling than the neighboring less diluted parcels. Because the criterion for cloud top entrainment instability [i.e., the CTEI criterion, Eq. (8)] was satisfied for all horizontal penetrations, it is highly plausible that entrainment-induced vertical circulation mixing could have taken place in these clouds, as exemplified in *Wang et al*. [2009]. As the cloud parcel descends, cloud droplets evaporate to maintain water vapor saturation but eventually at a certain altitude the droplets evaporate completely. This would be the local cloud base altitude. The descent may not stop here and proceed further down. If the parcel ascends again, its lifting condensation level would be probably close to its original local cloud base altitude. Importantly, if the descending parcels from cloud top are more diluted, evaporation of cloud droplets would be faster for these parcels and therefore the local cloud base altitude would be higher. This suggests that the cloud base altitude may not be uniform for an extensive stratocumulus cloud. Moreover, during the vertical circulation these parcels would mix with the surrounding parcels of different dilution and mixing history.

Therefore, it is necessary to consider the influence of vertical circulation mixing and its resultant cloud base altitude variation on the results of the mixing diagram analysis. In fact, the reason for the dominantly positive $\Gamma_{V\text{-}L}$ in Table 2 and Fig. 11 could be attributed simply to the faster evaporation of cloud droplets and/or shorter height from cloud base for more diluted (i.e., lower L) parcels. The strongly positive $\Gamma_{N\text{-}L}$ can also be explained by lower N for more diluted parcels. However, N can also be affected by new droplet activation for ascending parcels. The data points at the lower right corner in Fig. 9b may be from the sections of the cloud that have high cloud base altitudes but somehow have high number of activated droplets. Table 3 shows that there are 43 such 20 s segments from O17, O26 and O28. Table 3 also shows that the distinct HM like feature (i.e., $\Gamma_{N\text{-}V} > 0$) is not infrequently found when the variation of L is relatively large in a 20 s segment (47 segments). This could also be explained by faster evaporation of droplets in more diluted cloud parcels.

As shown in Table 3 there are 10 segments that might suggest further growth after IM. All of them are from P1 of O17. Unlike with the other penetrations examined in this study, P1 of O17 was close to cloud top (2.5 mb from cloud top, Table 1) and thus it is unlikely that this feature is caused by further growth after IM - the distance is too short. Instead at such a cloud altitude a negative $\Gamma_{V\text{-}L}$ could be generated according to the vertical circulation mixing hypothesis [*Wang et al*., 2009]: some droplets in the ascending but mixing-diluted parcels could grow faster and become larger than the droplets in less diluted parcels by the time they arrive near cloud top. Indeed *Wang et al*. [2009] observed that the correlation between liquid water mixing ratio and mean diameter of cloud droplets was negative for horizontal penetrations near cloud top but positive for penetrations into the mid-levels of stratocumulus clouds. This is similar to the contrast of $\Gamma_{V\text{-}L}$ values between P1 of O17 and the other penetrations in Table 2.

On account of these considerations we speculate that the mixing of entrained air near cloud top was indeed (dominantly) inhomogeneous as the scale parameters (J^* and J_L) indicate (Fig. 12 and Table 4). While during their descent, the cloud droplets would evaporate faster in more diluted parcels, eventually producing the prevalent HM trait observed at a significant depth from cloud top (on average 10.6 mb down from the cloud top in Table 1 when P1 of O17 is excluded). These parcels mix with neighboring parcels of different dilution during vertical circulation changing the cloud microphysical relationship accordingly, and near cloud top altitudes the correlation between V and L can even turn out to be negative as the P1 of O17 shows.

The final important thing to note is that in Table 2 the linear regressions for each penetration of the 1 Hz data show similar trends to those for individual 20 s segments of the 40 Hz data. That is, the cloud microphysical relationships established for 2 km horizontal length with ~2.5 m resolution data are similar to those established for much longer horizontal length (> 20 km) with ~100 m resolution data. The self-similar nature of these linear regressions over the very different spatial scales may imply that the mixing mechanism itself is not the crucial reason for these relationships. Whether IM or HM dominates would depend on the values of relevant scale parameters (J^* or J_L) but they are not determined by the averaging spatial scale of the data [See Eqs. (9) and (10)]. So if the apparent HM trait shown for the 40 Hz data (i.e., $\Gamma_{V\text{-}L} > 0$) were indeed due to HM, it would mean that HM is a mixing mechanism that is intrinsically identifiable on this scale. Then the apparent HM trait also shown for the 1 Hz data (i.e., the dominantly positive $\Gamma_{V\text{-}L}$ values in Table 2) can actually be considered as counter-evidence for HM. Even more remarkably in Table 2 the Γ values for individual 1 s segments of the 40 Hz data are similar to those for 20 s segments. That is, 100 m horizontal length is long enough to establish the shown relationships. This self-similarity of the cloud microphysical relationships may be explained if the vertical circulation mixing induced by cloud top entrainment and mixing is assumed to be the major reason for the relationships at the measurement altitudes. It can be speculated that vertical circulation mixing occurs on a scale that is identifiable at 40 Hz but it is embedded in much larger scale vertical circulation mixing identifiable at 1 Hz.

6. Summary and conclusions

Cloud microphysical data obtained from aircraft measurement of extensive stratocumulus clouds during the VOCALS-Rex field campaign were analyzed to find the evidence for the dominant mixing mechanism of the entrained dry air from above the cloud top. The mixing diagram analysis was made for the horizontal penetration data recorded at 1 Hz but it was found to be difficult to apply this method to the extensive stratocumulus clouds that were unlikely to have a single adiabatic cloud droplet concentration (N_a) and thus a single adiabatic cloud droplet mean volume (V_a). Moreover, entrainment interfacial layer (EIL) existed in most vertical soundings through the cloud layers. With no clear justification mid-level of EIL was assumed to be the source altitude of the entrained air. In addition, the data pattern seen in the mixing diagram suggested that the cloud base altitude was not uniform over the path. In an effort to minimize these problems, the 40 Hz data were used and the data subdivided into 20 s segments. Even in the mixing diagrams for such short cloud paths (~2 km length), the cloud parcel with the maximum N (equivalently N_a) was never identical to that of the maximum V (equivalently V_a), suggesting multiple number of N_a and thus V_a.

Despite this complexity, some important findings were made from the mixing diagram analyses. The dominant feature was the positive relationship identified between V and liquid water content (L): 293 out of 303 20 s segments showed such relationship. That is, for almost all segments the mean volumes of the droplets were larger for less diluted cloud parcels and not the other way around. This was a trait that would definitely be interpreted as homogeneous mixing but estimation of the relevant scale parameters (i.e., transition length scale and transition scale number) consistently suggested inhomogeneous mixing. We found that this dire discrepancy could be reconciled when it was taken into account that the horizontal penetration altitudes were significantly below the cloud top (on average 10.6 mb down) except one case that penetrated near the cloud top (2.5 mb down) and showed one of the few non-positive relationships between V and L. We speculate that the mixing of the entrained air near the cloud top may indeed have been dominantly inhomogeneous as the scaling parameter analysis suggested. The explanation being that during the descent of these entrainment affected and diluted cloud parcels, droplets would evaporate and, importantly, this evaporation would be faster for the more diluted cloud parcels. If so, the correlation between V and L can become positive at the altitudes of the mid-cloud penetrations, regardless of the mixing mechanism at cloud top. These descending parcels can also mix with ascending adjacent parcels and, because of the dilution caused by these parcels, some of the larger droplets in the mixed parcels might grow even faster during the ascent, eventually becoming larger than the ones produced without mixing near cloud top as demonstrated by *Wang et al*. [2009].

The vertical circulation mixing postulated here is a plausible scenario that is supported by the fact that the cloud top entrainment instability criterion was satisfied for the clouds analyzed in this study. Thus we are forced to conclude that the evidence for homogeneous mixing or inhomogeneous mixing based on analysis of the mixing diagram seems intrinsically problematic because the mixed parcels do not necessarily stay where the mixing occurred and experience vertical circulation and further mixing and therefore a mixing history that needs to be included in the analysis as well. The aircraft measurements furnish a transient picture of cloud microphysical relationships that are modulated by entrainment and mixing near cloud top and subsequent vertical circulation mixing in these long lasting stratocumulus clouds. Nevertheless, the suggestion made here must remain speculative until more supporting evidence is accumulated. Designing flight plans aimed at observing vertical variation of cloud microphysical relationships (i.e., horizontal penetrations through several different altitudes of the same stratocumulus deck) certainly would be promising in this effort. As explained earlier, an expected feature of vertical circulation mixing is the variation of local cloud base altitude: higher for more diluted parcels and vice versa. In this sense, identifying cloud base altitude is crucially important although it is difficult and often ignored in aircraft observations. Lastly from the 40 Hz data (~2.5 m resolution) it was found that 100 m horizontal length was long enough to establish the cloud microphysical relationships that were consistent with those for 2 km horizontal length. The question is whether the major reason for the cloud microphysical relationships described here is due to vertical circulation mixing, the scale of which is identifiable at only 100 m length. This is a question that should also be addressed in future studies.

Acknowledgments. This work is funded by the Korea Meteorological Administration Research and Development Program under Grant CATER_2012-3051. The authors would like to thank the flight crews of the G-1 aircraft during the VOCALS-Rex campaign. The data for this work are from the data archive maintained by Brookhaven National Laboratory [contact: Stephen Springston (srs@bnl.gov) or Gunnar Senum (gsenum@bnl.gov)]. BNL authors also thank the DOE Atmospheric Systems Research Program (ASR) for support.

References

Baker, M. B., R. G. Corbin, and J. Latham (1980), The influence of entrainment on the evolution of pcloud-droplet spectra: I. A model of inhomogeneous mixing, *Quart. J. R. Meteorol. Soc.*, *106*, 581–598.

Beard, K. V., and H. T. Ochs (1993), Warm-Rain Initiation: An Overview of Microphysical Mechanisms, *J. Appl. Meteorol.*, *32*, 608–625.

Blyth, A. M., and J. Latham (1985), An airborne study of vertical structure and microphysical variability within a small cumulus, *Quart. J. R. Meteorol. Soc.*, *111*, 773–792.

Burnet, F., and J.-L. Brenguier (2007), Observational Study of the Entrainment-Mixing Process in Warm Convective Clouds, *J. Atmos. Sci.*, *64*, 1995–2011.

Cooper, W. A. (1989), Effects of Variable Droplet Growth Histories on Droplet Size Distributions. Part I: Theory, *J. Atmos. Sci.*, *46*, 1301–1311.

Deardorff, J. W. (1980), Cloud Top Entrainment Instability, *J. Atmos. Sci.*, *37*, 131–147.

Devenish, B. J., and Coauthors (2012), Droplet growth in warm turbulent clouds, *Quart. J. R. Meteorol. Soc.*, *138*, 1401–1429, doi:10.1002/qj.1897.

Gerber, H., S. P. Malinowski, J.-L. Brenguier, and F. Burnet (2005), Holes and Entrainment in Stratocumulus, *J. Atmos. Sci.*, *62*, 443–459.

Gerber, H., G. M. Frick, J. B. Jensen, and J. G. Hudson (2008), Entrainment, mixing, and microphysics in trade-wind cumulus, *J. Meteorol. Soc.Japan*, *86A*, 87–106.

Grabowski, W. W., and L.-P. Wang (2009), Diffusional and accretional growth of water drops in a rising adiabatic parcel: Effects of the turbulent collision kernel, *Atmos. Chem. Phys.*, *9*, 2335–2353.

Grabowski, W. W., and L.-P. Wang (2013), Growth of cloud droplets in a turbulent environment, *Annu. Rev. Fluid Mech.*, *45*, 293–324.

Haman, K. E., S. P. Malinowski, M. J. Kurowski, H. Gerber, and J.-L. Brenguier (2007), Small scale mixing processes at the top of a marine stratocumulus—A case study, *Quart. J. R. Meteorol. Soc.*, *133*, 213–226, doi:10.1002/qj.5.

Hudson, J. G., S. S. Yum (1997), Droplet Spectral Broadening in Marine Stratus, *J. Atmos. Sci.*, *54*, 2642–2654.

Jensen, J. P., P. H. Austin, M. B. Baker, and A. M. Blyth (1985), Turbulent mixing, spectral evolution, and dynamics in a warm cumulus cloud, *J. Atmos. Sci., 42*, 173-192.

Kleinman, L., P. H. Daum, Y.-N. Lee, E. R. Lewis, A. J. Sedlacek III, G. I. Senum, S. R. Springston, J. Wang, J. Hubbe, J. Jayne, Q. Min, S. S. Yum, and G. Allen (2012), Aerosol concentration and size distribution measured below, in, and above cloud from the DOE G-1 during VOCALS-Rex, *Atmos. Chem. Phys.*, *12*, 207-223.

Lasher-Trapp, S. G., W. A. Cooper, and A. M. Blyth (2005), Broadening of droplet size distributions from entrainment and mixing in a cumulus cloud, *Quart. J. R. Meteorol. Soc*., *131*, 195–220.

Lehmann, K., H. Siebert, and R. A. Shaw (2009), Homogeneous and Inhomogeneous Mixing in Cumulus Clouds: Dependence on Local Turbulence Structure, *J. Atmos. Sci*., *66*, 3641–3659.

Lu, C., Y. Liu, and S. Niu (2011), Examination of turbulent entrainment-mixing mechanisms using a combined approach, *J. Geophys. Res*., *116*, D20207, doi:10.1029/2011JD015944.

McGraw, R. and Y. Liu (2003), Kinetic potential and barrier crossing: A model for warm cloud drizzle formation, *Phys. Rev. Letts. 90*, 18501, 1-4.

McGraw, R. and Y. Liu (2004), Analytic formulation and parameterization of the kinetic potential theory for drizzle formation, *Phys. Rev. E 70*, 031606.

McGraw, R. and Y. Liu (2006), Brownian drift-diffusion model for evolution of droplet size distributions in turbulent clouds, *Geophys. Res. Letts. 33*, L03802, doi:10.1029/2005 GL023545.

Paluch, I. R., (1979), The entrainment mechanism in Colorado cumuli, *J. Atmos. Sci., 36*, 2467-2478.

Paluch, I. R., and C. A. Knight (1984), Mixing and the Evolution of Cloud Droplet Size Spectra in a Vigorous Continental Cumulus, *J. Atmos. Sci., 41*, 1801–1815.

Paluch, I. R., and C. A. Knight (1986), Does Mixing Promote Cloud Droplet Growth?, *J. Atmos. Sci., 43*, 1994–1998.

Pawlowska, H., J.-L. Brenguier, and F. Burnet (2000), Microphysical properties of stratocumulus clouds, *Atmos. Res.*, *55*, 15–33.

Poellot, M. R., and C. A. Grainger (1991), A comparison of several airborne measures of turbulence, paper presented at the 4th International Conference of the Aviation Weather Systems, Am. Meteorol. Soc., Paris, France.

Randall, D. A. (1980), Conditional instability of the first kind upsidedown, *J. Atmos. Sci.*, *37*, 125–130.

Rogers, R.R., and M. K. Yau (1989), *A Short Course in Cloud Physics*, 3rd ed., 290pp., Pergamon, New York.

Seifert, A., and B. Stevens (2010), Microphysical Scaling Relations in a Kinematic Model of Isolated Shallow Cumulus Clouds, *J. Atmos. Sci.*, *67*, 1575–1590.

Telford, J. W., and S. K. Chai (1980), A new aspect of condensation theory, *Pure Appl. Geophys., 118,* 720-742.

Vaillancourt, P. A., M. K. Yau, P. Bartello, and W. W. Grabowski (2002), Microscopic Approach to Cloud Droplet Growth by Condensation. Part II: Turbulence, Clustering, and Condensational Growth, *J. Atmos. Sci.*, *59*, 3421–3435.

Wang, J., P. H. Daum, S. S. Yum, Y. Liu, G. I. Senum, M.-L. Lu, J. H. Seinfeld, and H. Jonsson (2009), Observations of marine stratocumulus microphysics and implications for processes controlling droplet spectra: Results from the Marine Stratus/Stratocumulus Experiment, *J. Geophys. Res.*, *114*, D18210, doi:10.1029/2008JD011035.

Wang, L.-P. and W. W. Grabowski (2009), The role of air turbulence in warm rain initiation, *Atmos. Sci. Lett.*, *10*, 1–8.

Warner, J. (1973), The Microstructure of Cumulus Cloud: Part IV. The Effect on the Droplet Spectrum of Mixing Between Cloud and Environment, *J. Atmos. Sci.*, *30*, 256–261.

Wood, R., and Coauthors (2011), The VAMOS ocean–Cloud–Atmosphere–Land Study Regional Experiment (VOCALS-REx): Goals, platforms, and field operations, *Atmos. Chem. Phys.*, *11*, 627–654.

Wood, R., C. S. Bretherton, D. Leon, A. D. Clarke, P. Zuidema, G. Allen, and H. Coe (2011), An aircraft case study of the spatial transition from closed to open mesoscale cellular convection over the Southeast Pacific, *Atmos. Chem. Phys.*, *11*, 2341-2370.

Xue, Y., L.-P. Wang, and W. W. Grabowski (2008), Growth of cloud droplets by turbulent collision–coalescence, *J. Atmos. Sci.*, *65*, 331–356.

Yamaguchi, T., and D. A. Randall (2008), Large-eddy simulation of evaporatively driven entrainment in cloud-topped mixed layers, *J. Atmos. Sci.*, *65*, 1481–1504.

Yum, S. S., and J. G. Hudson (2001), Cloud microphysical relationships in warm clouds, *Atmos. Res.*, *57*, 81– 104.

Yum, S. S. (1998), *Cloud droplet spectral broadening in warm clouds: An observational and model study*, PhD thesis, University of Nevada, Reno, Nevada, USA, 191pp.

Table 1. Average values of important cloud parameters for each horizontal penetration calculated from the 1 Hz dataset. Here p_{CT} and p_{CB} are the estimated pressure altitudes of cloud top and cloud base, respectively. The meaning of all other parameters is explained in the text.

	Duration (s)	T (K)	p (mb)	$p-p_{CT}$ (mb)	$p_{CB}-p$ (mb)	L (gm^{-3})	N (cm^{-3})	V (μm^3)	L_d (gm^{-3})
O17									
P1	478	280.5	903.7	2.5	20.6	0.384	383.0	1956.4	0.004
P2	1203	281.1	917.9	15.7	13.7	0.166	393.7	820.3	0.002
O26									
P1	533	281.2	906.9	9.2	7.0	0.079	324.6	197.8	0.002
P2	1441	280.2	889.8	22.9	4.9	0.177	201.1	739.3	0.007
P3	478	279.8	879.5	6.9	22.4	0.255	197.5	1002.3	0.008
P4	312	282.3	895.7	9.0	9.4	0.104	248.1	366.3	0.010
O28									
P1	483	281.4	881.2	11.9	11.5	0.335	264.7	1290.0	0.047
P2-1	261	281.4	883.9	5.6	24.1	0.120	170.1	716.6	0.007
P2-2	198	281.4	887.1	8.8	20.9	0.223	175.9	1015.8	0.015
P3	483	280.4	882.8	8.9	24.5	0.191	180.2	969.0	0.004
P4-1	267	278.8	871.1	7.1	20.9	0.186	153.5	1188.4	0.004
P4-2	166	278.8	873.2	9.2	18.8	0.345	135.6	2515.8	0.050
P5	451	279.2	869.4	10.0	30.9	0.498	94.9	5098.2	0.343
P6	653	280.0	872.7	12.7	30.3	0.470	139.0	6532.9	0.134

Table 2. Averages and standard deviations for each horizontal penetration of the correlation coefficients (Γ) of the linear regressions between N and V, N and L, and V and L for individual 20 s segments (40 Hz) and the same correlation coefficients for all data in each horizontal penetration (1 Hz).

	40Hz			1Hz		
	$\Gamma_{N\text{-}V}$	$\Gamma_{N\text{-}L}$	$\Gamma_{V\text{-}L}$	$\Gamma_{N\text{-}V}$	$\Gamma_{N\text{-}L}$	$\Gamma_{V\text{-}L}$
O17						
P1	-0.35±0.40	0.88±0.10	0.04±0.38	-0.48	0.91	-0.09
P2	-0.51±0.30	0.03±0.47	0.76±0.28	-0.33	0.21	0.84
O26						
P1	-0.14±0.19 (-0.10±0.32)	0.18±0.16 (0.26±0.36)	0.91±0.11 (0.90±0.11)	-0.03	0.18	0.97
P2	-0.15±0.22 (-0.09±0.28)	0.48±0.26 (0.59±0.29)	0.74±0.15 (0.69±0.18)	0.20	0.40	0.97
P3	-0.21±0.32 (-0.10±0.30)	0.66±0.15 (0.73±0.18)	0.53±0.16 (0.55±0.19)	-0.43	0.12	0.89
P4	-0.62±0.05 (-0.35±0.28)	-0.11±0.11 (-0.13±0.33)	0.82±0.03 (0.79±0.21)	-0.80	-0.53	0.90
O28						
P1	-0.30±0.22 (-0.12±0.27)	0.48±0.27 (0.60±0.23)	0.65±0.09 (0.68±0.16)	-0.34	0.14	0.87
P2-1	-0.29±0.27 (-0.16±0.37)	0.34±0.29 (0.46±0.38)	0.73±0.08 (0.72±0.17)	-0.65	-0.35	0.91
P2-2	-0.22±0.35 (-0.17±0.36)	0.55±0.20 (0.57±0.28)	0.61±0.14 (0.64±0.21)	-0.06	0.46	0.84
P3	-0.13±0.17 (-0.04±0.31)	0.64±0.17 (0.70±0.20)	0.63±0.14 (0.63±0.17)	-0.36	0.02	0.92
P4-1	0.06±0.30 (0.05±0.34)	0.83±0.06 (0.82±0.13)	0.54±0.16 (0.57±0.21)	-0.27	0.47	0.71
P4-2	-0.03±0.27 (-0.06±0.26)	0.78±0.08 (0.80±0.12)	0.55±0.14 (0.50±0.18)	0.04	0.66	0.77
P5	0.04±0.18 (0.02±0.22)	0.84±0.10 (0.86±0.09)	0.53±0.09 (0.49±0.19)	-0.06	0.79	0.57
P6	-0.18±0.20 (-0.06±0.21)	0.74±0.17 (0.80±0.12)	0.48±0.08 (0.52±0.17)	-0.26	0.66	0.54

Table 3. Expected correlation coefficients for some dominant cloud microphysical processes and the number of 20 s segments that show such characteristics.

Dominant process	$\Gamma_{N\text{-}V}$	$\Gamma_{N\text{-}L}$	$\Gamma_{V\text{-}L}$	No. of segments
HM	> 0	> 0	> 0	47
IM	~ 0	> 0	~ 0	0
Further growth after IM	< 0	> 0	< 0	10
Many recently activated droplets	< 0	< 0	> 0	43
Small variation of L	< 0	> 0	> 0	169
Not classified	•	•	•	34

e 4. Statistical values (average, 5% percentile, median and 95% percentile) of the transition length scale (J^*) and transition scale number (J_L) for each penetration.

		Ave	5%	Median	95%
J^* (cm)	O26				
	P1	0.021	0.002	0.013	0.065
	P2	0.085	0.007	0.054	0.266
	P3	0.135	0.021	0.104	0.356
	P4	0.043	0.002	0.031	0.126
	O28				
	P1	0.275	0.043	0.190	0.795
	P2-1	0.193	0.019	0.122	0.596
	P2-2	0.260	0.041	0.183	0.742
	P3	0.141	0.023	0.106	0.375
	P4-1	0.166	0.033	0.134	0.417
	P4-2	0.462	0.094	0.348	1.185
	P5	1.457	0.223	1.058	4.048
	P6	0.910	0.171	0.690	2.404
J_L	O26				
	P1	0.129	0.006	0.059	0.462
	P2	0.505	0.019	0.226	1.882
	P3	0.803	0.049	0.471	2.707
	P4	0.226	0.002	0.118	0.801
	O28				
	P1	1.503	0.107	0.761	5.282
	P2-1	1.074	0.052	0.524	3.915
	P2-2	1.383	0.098	0.722	4.792
	P3	0.779	0.055	0.440	2.556
	P4-1	0.933	0.079	0.573	2.996
	P4-2	2.883	0.237	1.607	9.345
	P5	9.860	0.557	4.956	34.317
	P6	5.873	0.467	3.346	19.776

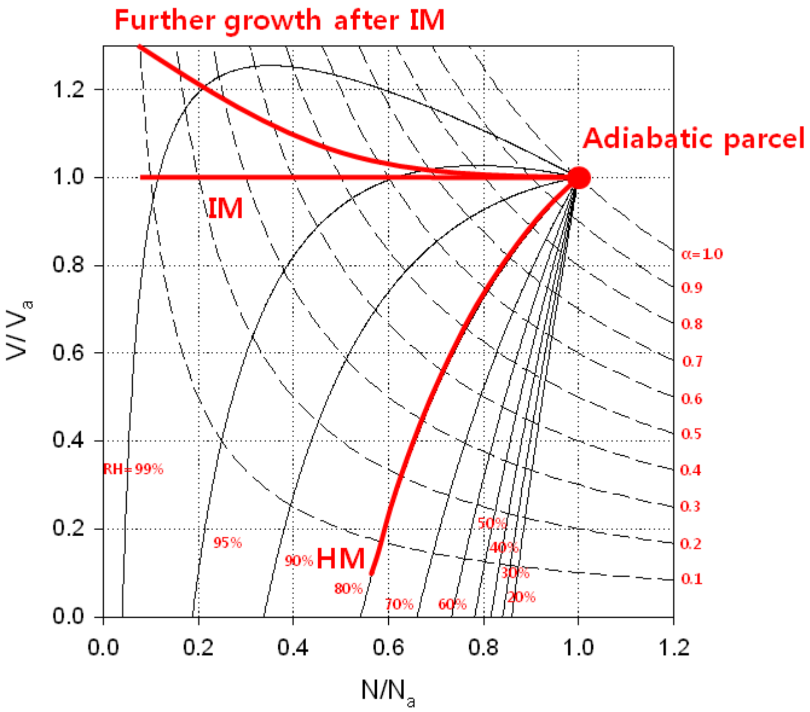

Figure 1. Example of a mixing diagram setting. Solid lines indicate the data scatter when cloud parcels mix homogeneously (HM) with the dry air that has the given relative humidity (RH). Dashed lines indicate iso-lines of liquid water dilution ratio (α). Expected features for inhomogeneous mixing (IM) and further growth after IM are also shown.

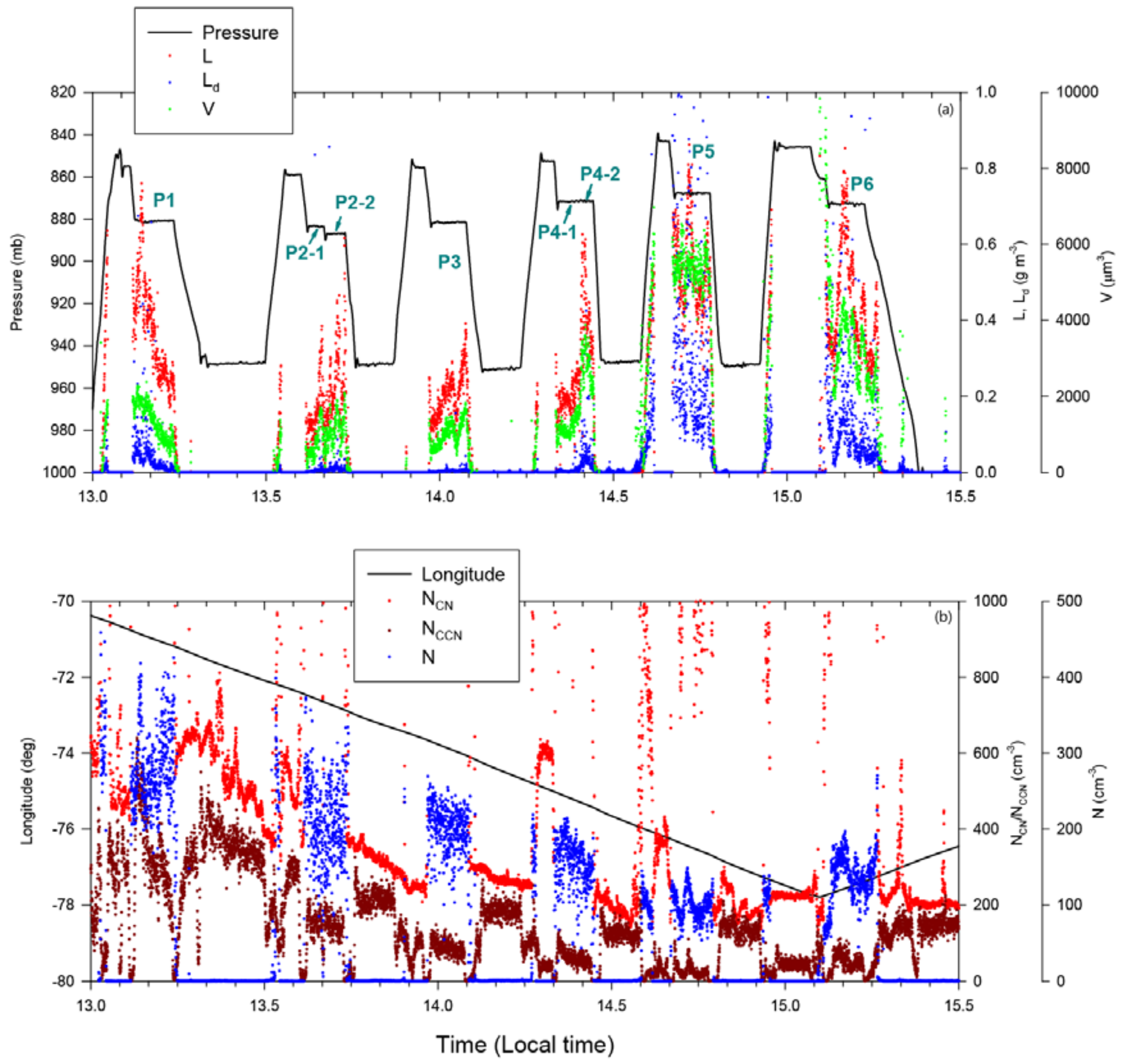

Figure 2. Time variation of important cloud parameters, and pressure altitude and longitude during the flight on October 28, 2008 (O28) (from 1 Hz dataset). Horizontal penetration numbers are marked as shown.

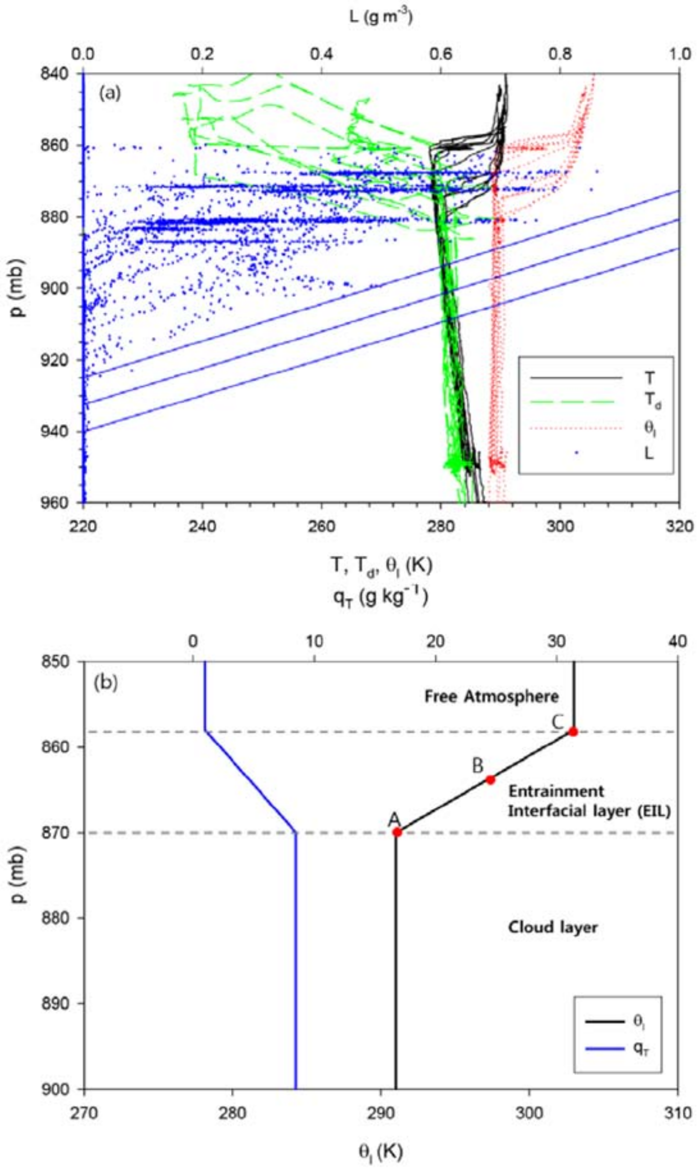

Figure 3. (a) All vertical profiles of the thermodynamic variables (T, T_d and θ_l) and liquid water content (L) observed on the October 28 flight and (b) representative vertical profiles of θ_l and total water mixing ratio (q_T) for this flight. Also shown in (a) are three adiabatic L profiles starting from three different cloud base heights for reference. A, B and C mark the hypothetical source altitudes of entrained air that indicate the bottom, middle and top of the EIL, respectively.

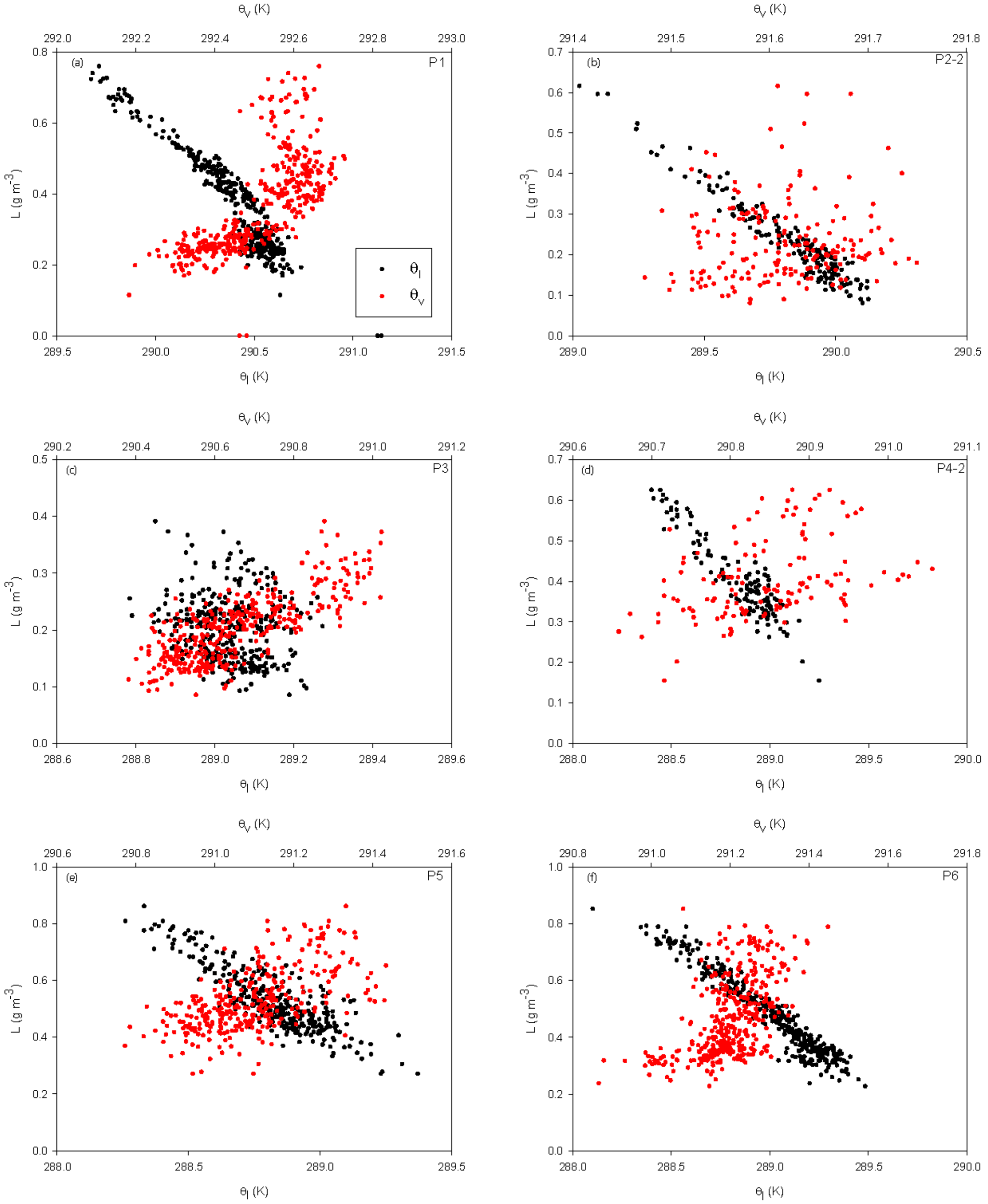

Figure 4. Liquid water potential temperature (θ_l) and virtual potential temperature (θ_v) as a function of liquid water content (L) for each horizontal penetration in O28 explained in Table 1 (from 1 Hz dataset). The penetration numbers are written at the upper right corner. For brevity only one subdivided part is selected from P2 and P4.

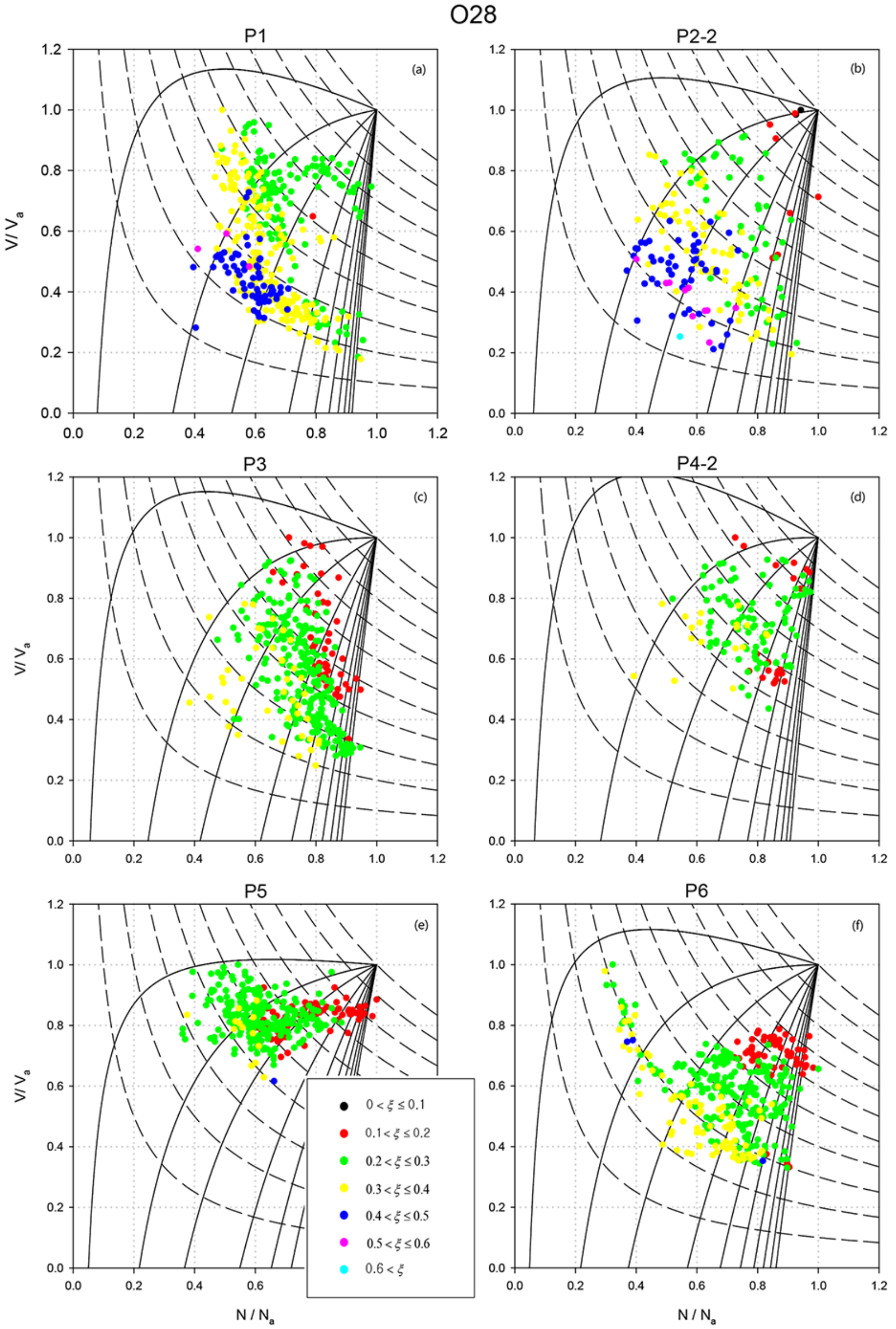

Figure 5. Mixing diagram for each horizontal penetration in O28 explained (from 1 Hz dataset). The color scales indicate ξ values that signify dispersion value. The penetration numbers are identical to those in Fig. 4.

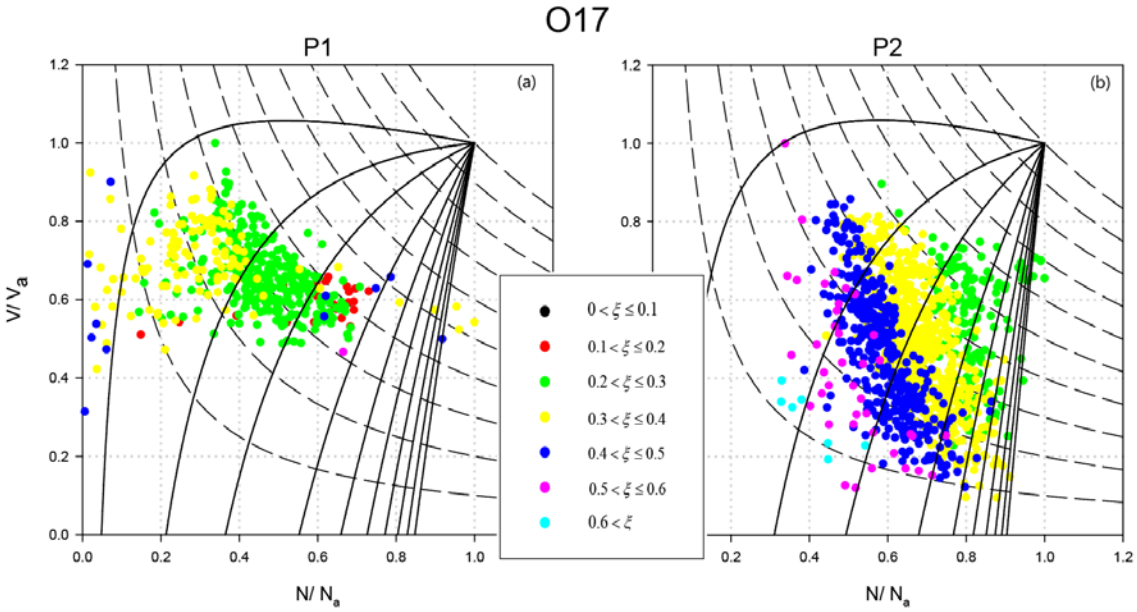

Figure 6. Same as Fig. 5 except for O17.

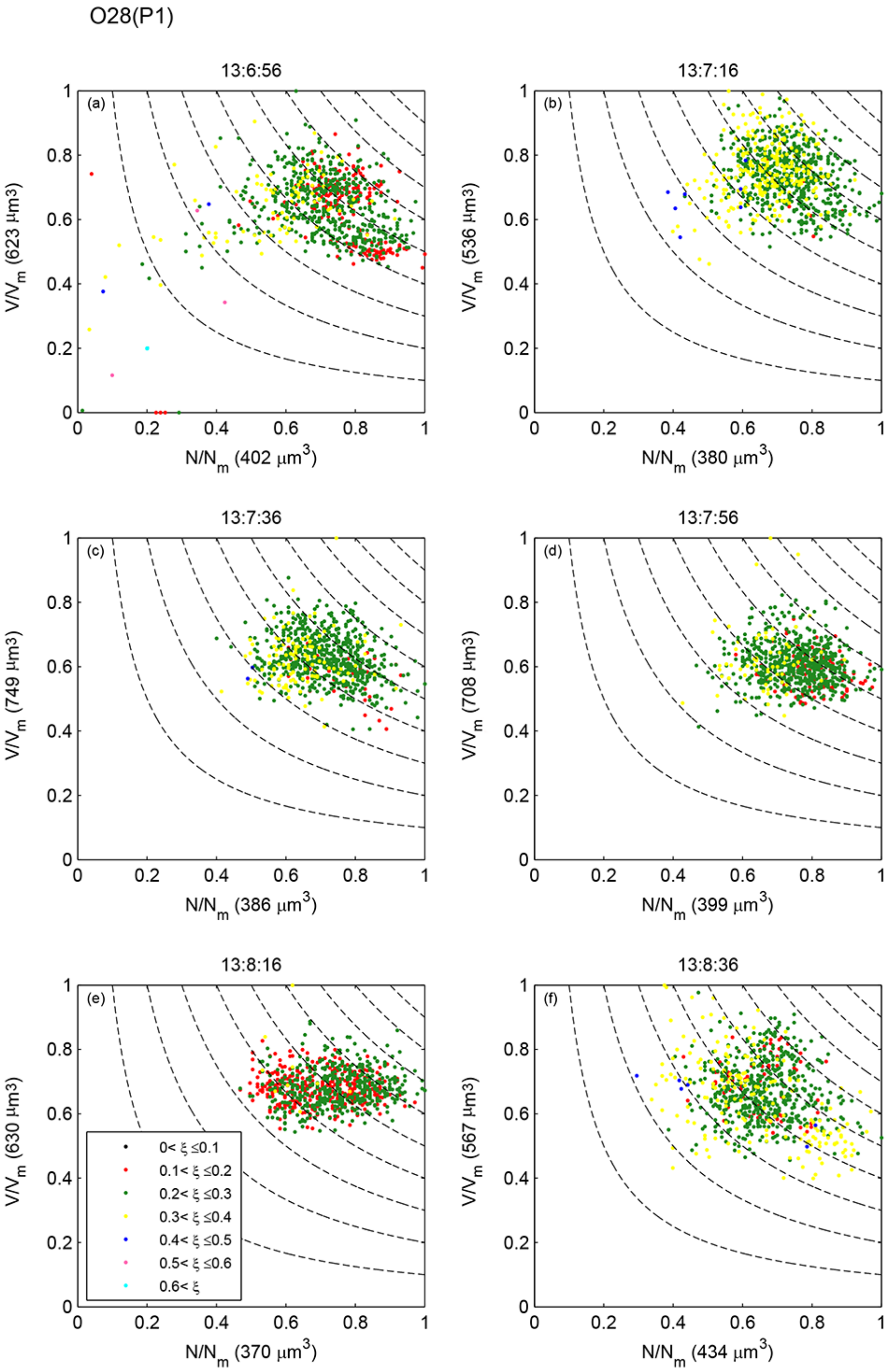

Figure 7. Mixing diagrams for six consecutive 20 s segments of the horizontal penetration 1 (P1) of O28 (from 40 Hz dataset). The starting time of each 20 s segments are marked on top of each panel and the numbers in parentheses in x and y axis labels indicate the maximum values, N_m and V_m, respectively, in the segment.

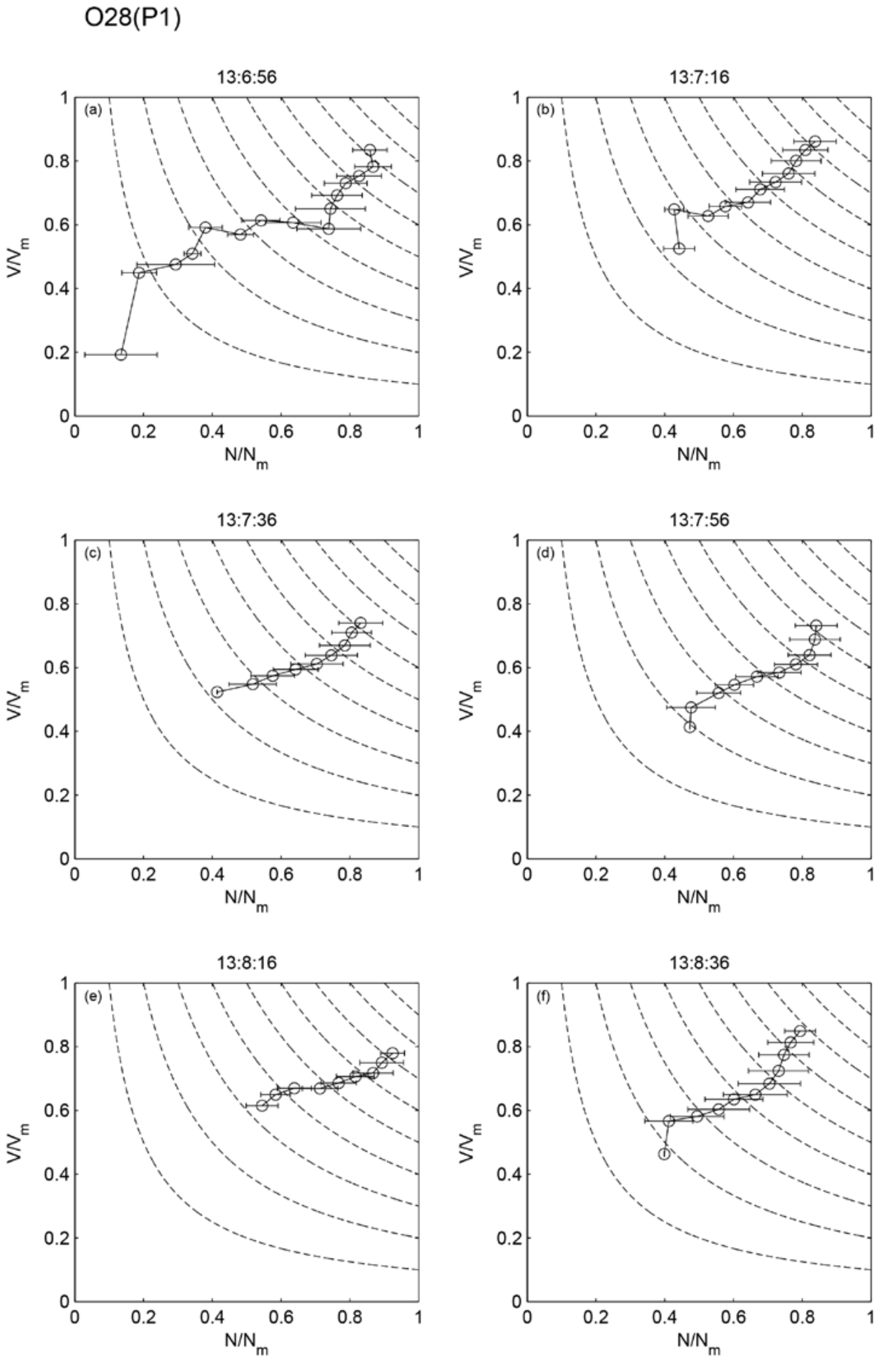

Figure 8. The α bin (0.05 interval) plots of the corresponding mixing diagrams in Fig. 7.

O28

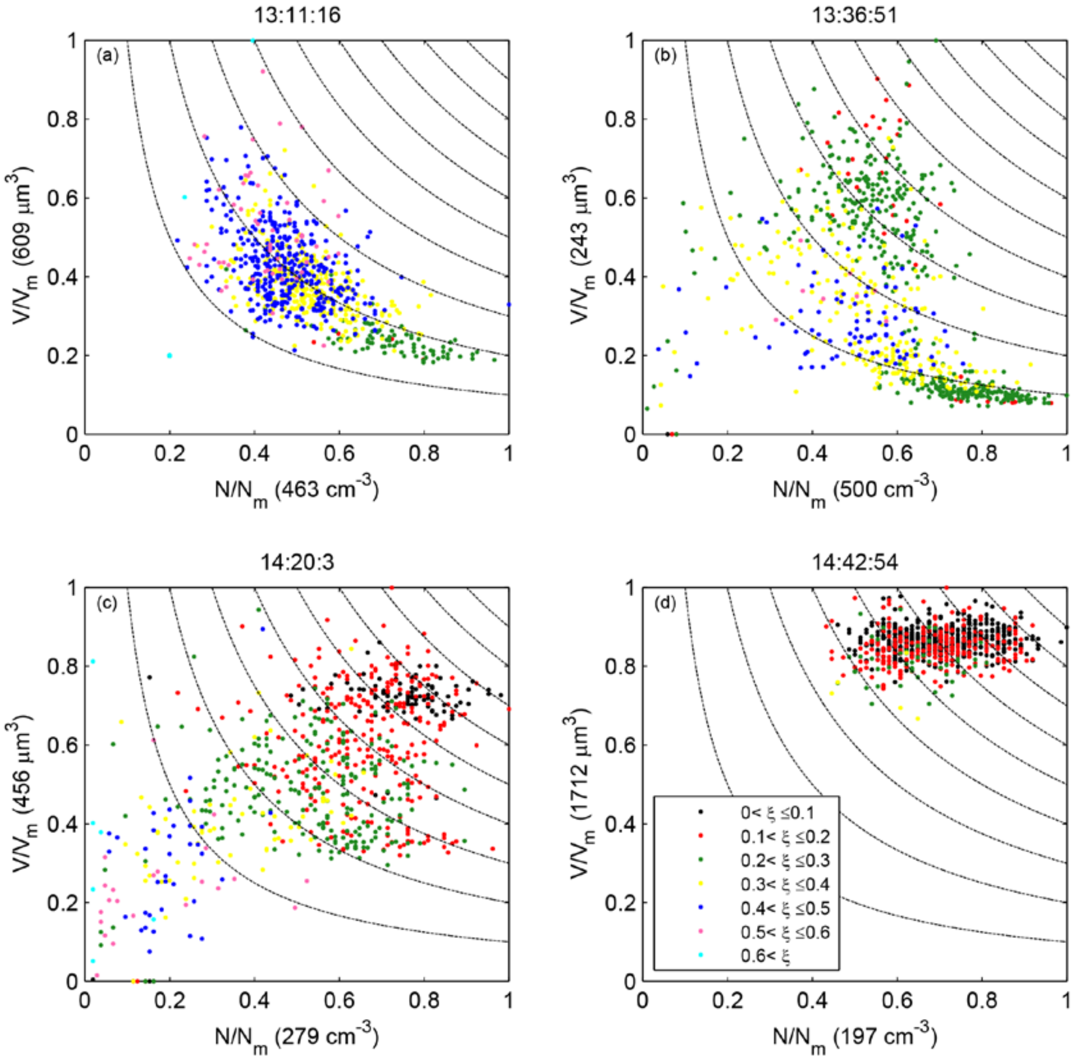

Figure 9. Frequently observed types of mixing diagrams from O26 and O28.

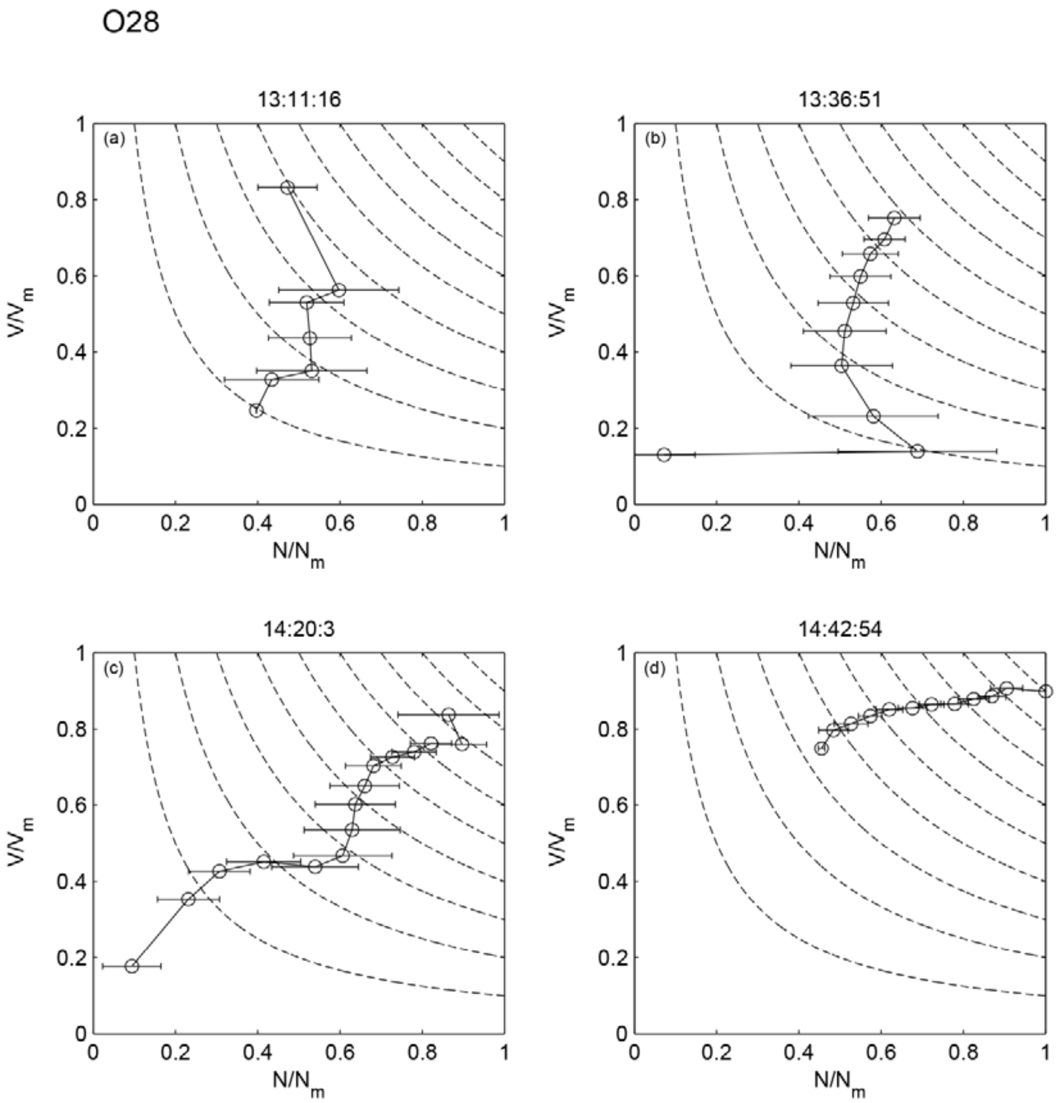

Figure 10. The α bin (0.05 interval) plots of the corresponding mixing diagrams in Fig. 9.

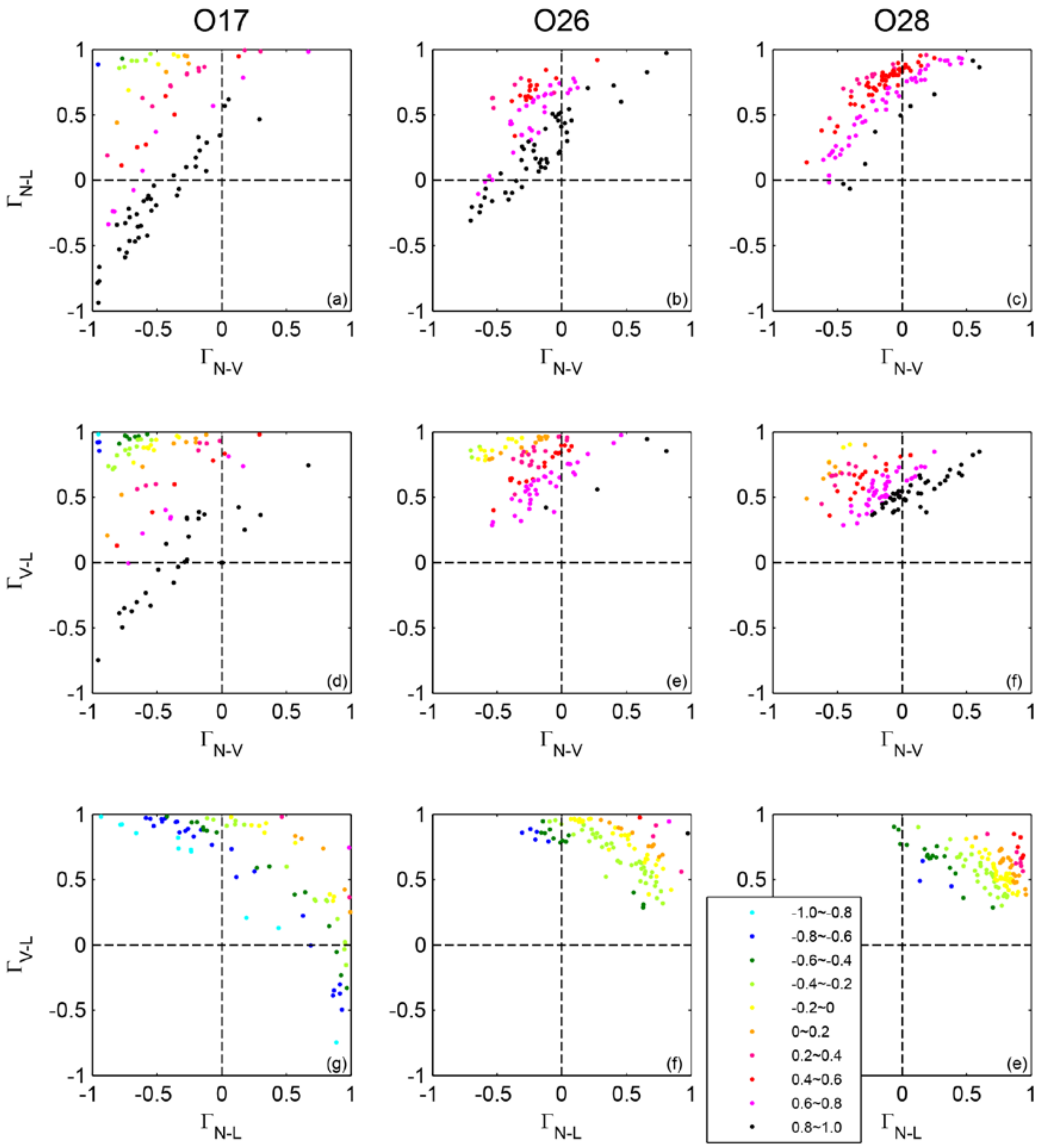

Figure 11. Scatterplots of $\Gamma_{N\text{-}V}$ vs. $\Gamma_{N\text{-}L}$, $\Gamma_{N\text{-}V}$ vs. $\Gamma_{V\text{-}L}$ and $\Gamma_{N\text{-}L}$ vs. $\Gamma_{V\text{-}L}$ for all data in each flight (O17, O26 and O28). The color scales indicate the Γ values of the remaining linear regression.

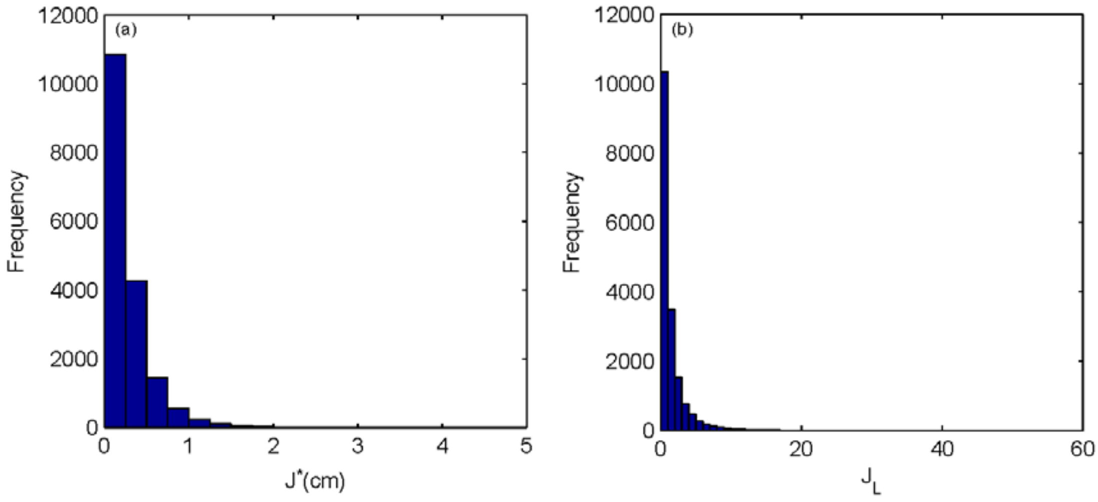

Figure 12. Distribution of (a) the transition length scale (J^*) and (b) transition scale number (J_L) of each 40 Hz data of the horizontal penetration 1 (P1) of O28.